

Chapter 5

Fabrication and characterization of doped-ZnO nanowires

5.1. Introduction

In this chapter, three important elements (Mg, Al, and In), which affect the ZnO nanostructures have been reported by several groups, are selected as dopants materials in ZnO nanowires. It described the role of these materials as dopant in ZnO is already described in Chapter Two.

Besides these reasons, new methods are applied for fabrication of these materials, which is caused to observe different behavior of these materials as impurity in ZnO nanostructures in comparison to the other reports. Therefore, conventional and modification set-up are applied to Mg-doped ZnO nanowires. Furthermore, effect of this modification on field emission characterization is investigated. Ultra AlN thin film is applied to Al-doped ZnO nanowires in a conventional set-up and sintering method is used to prepare the source material of In-doped ZnO nanowires.

5.2. Growth and characterization of $Zn_xMg_{1-x}O$ nanowires

5.2.1. Growth of $Zn_xMg_{1-x}O$ nanowires using a conventional set-up

In this section, a sintering method to prepare a $ZnO/Zn_xMg_{1-x}O$ compound as the source material is presented. The ZnO and $Zn_xMg_{1-x}O$ nanostructures were grown on silicon substrates at different temperatures, using gold metal as a catalyst in the presence of argon as a carrier gas in a conventional tube furnace. The effects of the substrate temperatures, gold catalyst, and source material preparation on the morphological and optical properties of the nanostructures are investigated.

5.2.1.1. Experimental details

Cleaning process of Si(100) substrates is similar the previous chapter. A gold layer of about 10 nm thickness, serving as a metal catalyst, was deposited on the substrates by a sputtering technique. Zinc oxide (99.99%) and magnesium powders (99.99%) were mixed at a molar ratio of 10:1, and then pressed into a small pill under a pressure of 40 MPa. The pill was calcined in a box furnace at 500 °C for 5 h and sintered at 900 °C for 12 h in the air, thereby producing a pill of the ZnO/ Zn_xMg_{1-x}O compound. After the heat treatment, the pill was ground into powder again. Then, the powder was placed on an alumina boat and inserted into a horizontal tube furnace, which served as the evaporation source. Silicon substrates were located downstream from the source material at 700 and 800 °C. A vacuum of 800 Pa was maintained inside the furnace tube during the deposition of the nanostructures. The source material was heated up to 1100 °C and was maintained at this temperature for 1 h. High purity Ar gas was fed at about 100 sccm into the furnace tube at one end, while the other end was connected to a rotary pump.

5.2.1.2 Results and discussion

To investigate the crystal structure of the source material (ZnO/Zn_xMg_{1-x}O), XRD pattern of the pill after sintering was determined. Figure 5.1 shows the XRD pattern of the pill. The observed diffraction peaks are quite similar to those of single-crystalline wurtzite hexagonal bulk ZnO, except for the two peaks at 42.80° and 62.15° that belong to cubic phase Zn_xMg_{1-x}O (Qiu *et al.*, 2008). In the XRD pattern for the pill, a slight shift of the (002) peak to a higher 2θ of 34.55° from 34.40° (the standard for bulk ZnO) was observed, indicating the substitution of the smaller Mg²⁺ ion

($r_{\text{Mg}^{2+}}=0.057$ nm) for Zn^{2+} ($r_{\text{Zn}^{2+}}=0.06$ nm). This pattern indicates that the source material has a two phases.

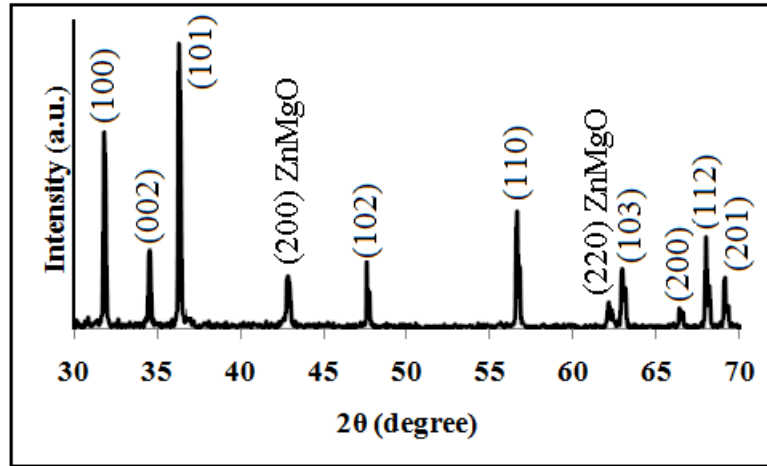


Figure.5.1. XRD pattern of the source material before evaporation. The observed diffraction peaks are quite similar to those of single-crystalline wurtzite hexagonal bulk ZnO, except for the two peaks at 42.80° and 62.15° that belong to the cubic phase of $\text{Zn}_x\text{Mg}_{1-x}\text{O}$.

Figure 5.2 (a) shows an FESEM image of the top view of the sample processed at 700°C . The morphology of the nanostructures produced in this temperature region consists of nanorods. In addition, the nanorods are quasi-aligned and semi-perpendicular to the substrate. Two types of nanorods were found in this sample, one being cubic ($\text{Zn}_x\text{Mg}_{1-x}\text{O}$) and the other being hexagonal (ZnO). Only a small number of nanorods of the cubic phase were produced because the quantity of Mg atoms in the source was less than that of the Zn atoms. In fact, the XRD pattern from Fig. 5.1 shows two independent phases (ZnO and $\text{Zn}_x\text{Mg}_{1-x}\text{O}$). The ZnO and $\text{Zn}_x\text{Mg}_{1-x}\text{O}$ may act in two independent roles as the sources materials are placed at the same position in the furnace. The typical average diameter and length of the nanorods obtained in the low temperature zone were about 50 nm and 1.5 μm , respectively. Figure 5.2 (b) shows a typical EDX spectrum of the top view of the nanorods grown on the substrate at 700°C . In this view, Zn, O, Mg, and Au peaks are detected. It can be observed that the amount of Mg in this view is very low.

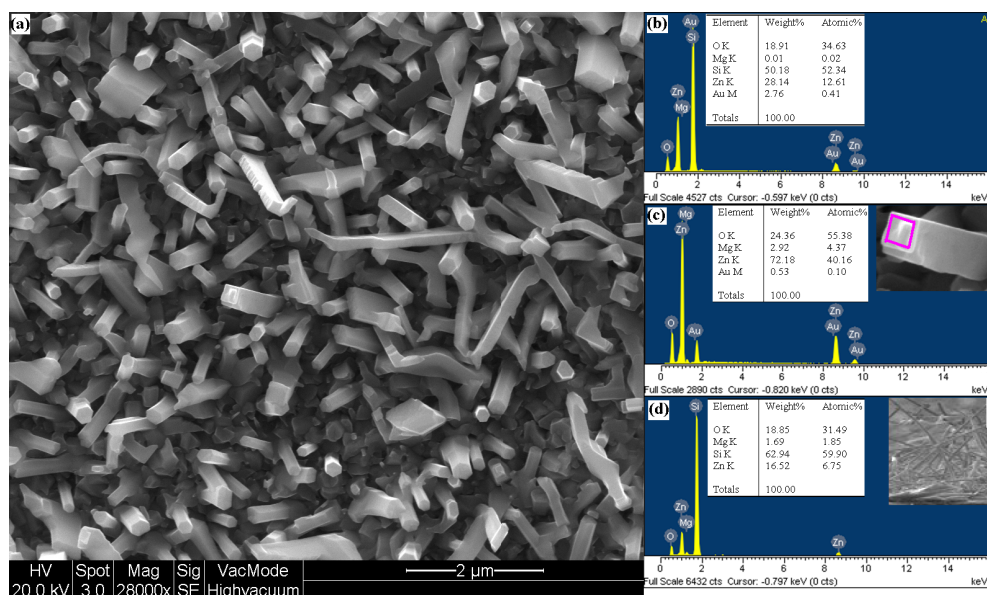


Figure 5.2. (a) FESEM image of the nanorods grown at 700 °C. (b) EDX spectrum of the top view of nanorods grown at 700 °C. (c) EDX spectrum and FESEM image of a single $Zn_xMg_{1-x}O$ nanowire with cubic shape. (d) EDX spectrum and FESEM image of a cross-sectional view of ZnO and $Zn_xMg_{1-x}O$ nanorods grown on a thin $Zn_{1-x}Mg_xO$ buffer layer deposited on a Si substrate at 700 °C.

Additionally, we selected some nanowires with hexagonal and cubic shapes for the EDX measurements; the EDX results showed that the nanowires with the hexagonal shape contained negligible Mg element, while the nanowires with the cubic shape contained a considerable amount of Mg element (Fig. 5.2 (c)). Furthermore, the percentage of Mg in a single nanowire with the cubic shape is higher than the average percentage of Mg obtained from the top view.

Based on the FESEM results were shown in Fig. 5.2, no Au particles were observed at the ends of the nanorods, but the EDX spectra of the top view and the single nanowire show Au peaks, so there may be gold particles close to the tips of the nanorods. It is possible that the nanorods grew by VLS and VS processes, whereby, initially, the nanorods grew through the VLS process but then continued to grow by the VS process. In fact, the Au dots on the nanorods could be located at three positions after growth: (1) on the top, (2) on the side and (3) on the bottom of the rods (Li *et al.* 2006).

Figure 5.2(d) shows an FESEM image and an EDX spectrum of a cross-sectional view of the sample produced at 700 °C. In this view, the EDX results clearly show Zn, O, Si, and Mg peaks along with their percentages. The EDX spectrum of the cross-section has been taken from an area about 40 μm in length and 15 nm in width. In fact, the EDX results of the cross-section show the formation of a thin $Zn_xMg_{1-x}O$ buffer layer that is located between the Si substrate and the nanorods. This measurement was taken from several regions of the cross-section. Some of these measurements showed the same results, but a few of them did not show an Mg peak. Therefore, these results indicate that the thin $Zn_xMg_{1-x}O$ buffer layer is not uniform. We did not observe any peaks for Au from the cross-section, so these results also confirm that the initial stage of nanorods growth occurred by the VLS process.

Figure 5.3(a) shows an FESEM image of the top view of the sample processed at 800 °C. The morphology of the nanostructures from this temperature region consists of nanosheets and nanorods.

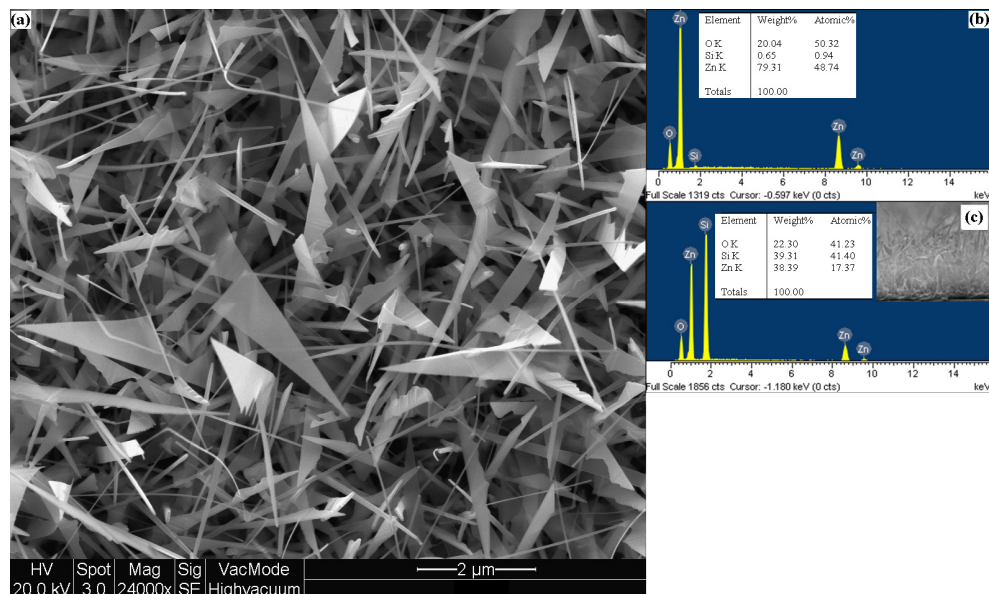


Figure 5.3. (a) FESEM image of nanosheets and nanorods grown at 800 °C. (b) EDX spectrum of the top view of the nanosheets and nanorods grown at 800 °C. (c) EDX and FESEM of the cross-sectional view of the ZnO nanosheets and nanorods grown on a Si substrate at 800 °C.

It can be observed that each nanosheet is constructed with a nanorod. Figure 5.3(b) shows an EDX spectrum of the top view of the sample produced at 800 °C. This spectrum detected Zn and O, while no peaks related to Mg or Au were observed. Figure 5.3(c) shows an FESEM image and an EDX spectrum of a cross-sectional view of the sample produced at 800 °C. The EDX result from this view also shows no peaks for Mg or Au.

Figures 5.4 (a-b) show the XRD patterns of the nanostructures grown on substrates at 700 and 800 °C, respectively. At 700 °C, the XRD diffraction of the sample not only shows ZnO peaks but also presents one peak at 38.20°, which belongs to the Au(111) catalyst. The peak of Au with (111) orientation appears in the sample at 700 °C because the first step of nanorods growth occurred by the VLS method, resulting in gold dots close to the tip of the nanorods.

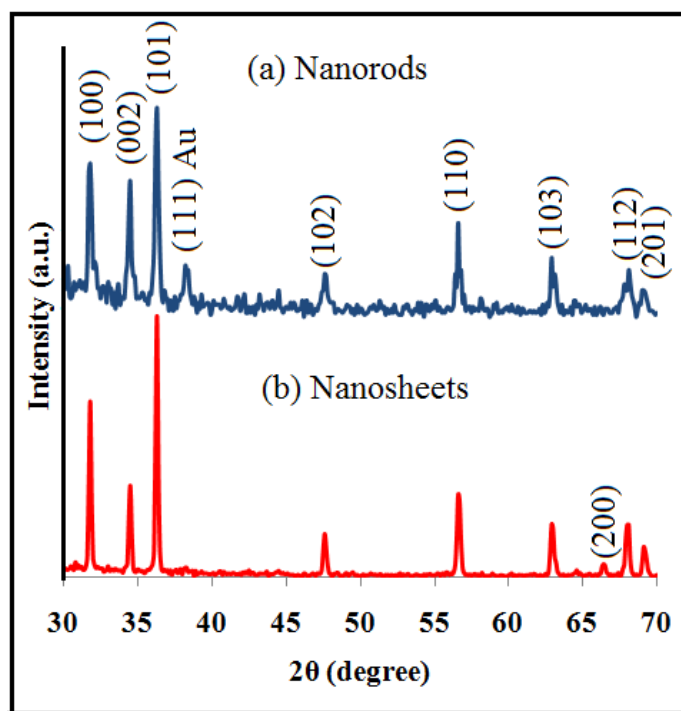


Figure 5.4. (a) XRD pattern of ZnO nanorods deposited at 700 °C. (b) XRD pattern of ZnO nanosheets grown on the Si at 800 °C. This pattern shows an additional peak of ZnO in comparison to the other sample at 66.3° (200).

The observed diffraction peaks of the sample at 800 °C (Fig. 5.4(b)) are quite similar to those of single-crystalline wurtzite hexagonal bulk ZnO. This pattern shows an additional ZnO (200) peak as compared to the XRD pattern of the sample at 700 °C. Such a peak appeared in the sample with nanosheet morphology because such morphology provides more surfaces of ZnO to be detected by the XRD.

Based on the obtained results, a growth mechanism of the ZnO and $Zn_xMg_{1-x}O$ nanostructures can be tentatively proposed. First, the ZnO/ $Zn_xMg_{1-x}O$ powders are initially transformed into corresponding vapors, namely $ZnO_x(g)$ and $Zn_xMg_{1-x}O(g)$ at the center of the furnace. These vapors are transferred to the low temperature zones by the carrier gas. Concurrently, the gold film on the substrate at 800 °C will start to evaporate, due to the volatile near-surface atoms of the gold thin films at high temperatures (Mensah *et al.*, 2007). In addition, the gold thin film on the substrate at 700 °C will transform to gold islands, since 700 °C is an optimum temperature for transforming gold thin films to gold islands (Fig. 3.6). At 800 °C, the gold vapors acting as catalysts capture and condense the $ZnO_x(g)$ into solids, thereby forming ZnO nanosheets. Since the gold vapors act as catalysts for condensing the $ZnO_x(g)$, they can diffuse anywhere within the nanostructures. Therefore, the EDX would not detect any gold for the sample with the nanosheet morphology. In fact, the growth of the nanosheets occurs via the VS process. In such a manner, the higher temperature and the larger supersaturation ratio facilitate 2D nucleation, resulting in the formation of the nanosheet structures (Dai *et al.*, 2003).

Moreover, it is possible that some of the gold vapors could be moved by the carrier gas to downstream of the sample that is placed at 800 °C and there react with the other ZnO_x vapors. Based on the FESEM results is shown in Fig. 5.2, the other morphologies of the ZnO nanostructures (the EDX results of these morphologies do not show any Mg peaks) could be attributed to this effect. It most likely that the $Zn_xMg_{1-x}O$.

$x\text{O}(\text{g})$ could not react with the Au vapors in the high temperature zone because the electron density of this compound is less than that of ZnO_x due to the existence of Mg, which has a weaker nucleus than Zn. The $\text{Zn}_x\text{Mg}_{1-x}\text{O}(\text{g})$ and the remainder of the $\text{ZnO}_x(\text{g})$ were transferred to the lower temperature region (700°C) and reacted in the presence of gold island catalysts on a substrate at 700°C , forming a thin $\text{Zn}_{1-x}\text{Mg}_x\text{O}$ buffer layer and nanorods. As the quantity of Mg is low in the source, a certain amount of Mg will produce a $\text{Zn}_{1-x}\text{Mg}_x\text{O}$ nanostructure as a thin buffer layer on the Si substrate, but after a while, there will only be $\text{ZnO}_x(\text{g})$ atoms and a few $\text{Zn}_x\text{Mg}_{1-x}\text{O}(\text{g})$ molecules. The $\text{ZnO}_x(\text{g})$ atoms react with the alloy of the thin Au- $\text{Zn}_{1-x}\text{Mg}_x\text{O}$ layer, so the ZnO and $\text{Zn}_x\text{Mg}_{1-x}\text{O}$ nanorods grow on this thin layer. In fact, Mg is diffused into a few nanorods, thereby producing a few $\text{Zn}_x\text{Mg}_{1-x}\text{O}$ nanorods with cubic shape. The cross-sections of a few of the ZnO nanorods are changed from hexagonal to triangular due to the presence of Mg precursors. The growth mechanism of the ZnO and ZnMgO nanostructures and the formation of the thin $\text{Zn}_{1-x}\text{Mg}_x\text{O}$ buffer layer on the Si substrates are schematically shown in Fig. 5.5.

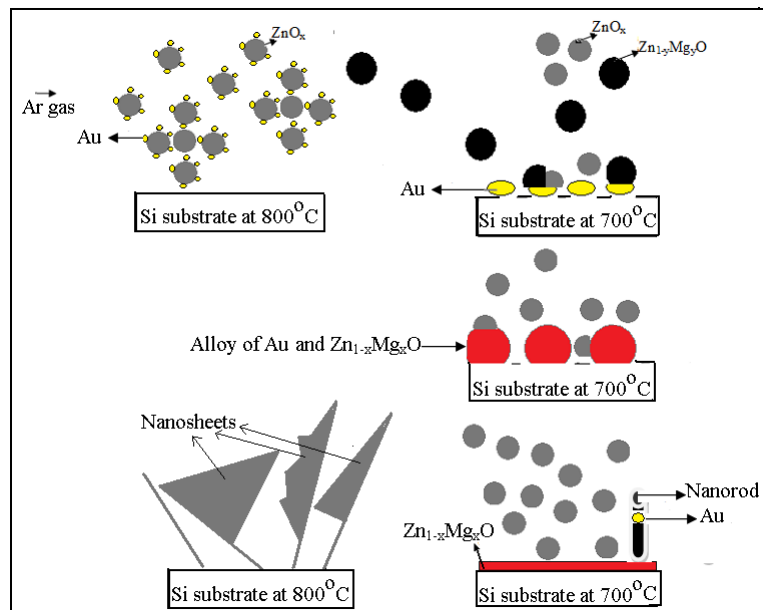


Figure 5.5. Thin $\text{Zn}_{1-x}\text{Mg}_x\text{O}$ buffer layer and the ZnO nanostructure growth process mechanism on Si substrates. This pattern shows two different roles of Au during the formation of the nanostructures.

Yang, A.L. *et al.* (2009), suggested that the growth rate along the c-axis changed little, while the growth of six equivalent facets of the type $\{10\bar{1}0\}$ of the $Zn_{1-x}Mg_xO$ increases with the addition of Mg. Surely, the $Zn_{1-x}Mg_xO$ layer is not uniform, therefore just a few of the cross-sections of the nanorods changed from hexagonal to triangular. Thus, the doping rate of Mg in the nanostructures can be changed to some extent by varying the distance between the source and the substrate in the furnace. By comparing the two types of grown nanostructures, we can see that Au has a significant role in the formation of the nanostructures. Actually, Au has two different roles in the growth of the nanostructures. One role is related to the vapor phase, which causes ZnO nanosheets to be obtained, and the other role is involved in the catalysis in the liquid phase on the Si substrate at 700 °C, which produces the $Zn_{1-x}Mg_xO$ thin layer and nanorods with a cubic shape.

Figure 5.6 shows the room temperature PL spectra of the nanorods and nanosheets. There are two bands in the PL spectra of the products; one of them is related to the UV emission at 378-382 nm and the other is related to the DLE at 508-522 nm. The strong green band in Fig. 5.6 shows that there are very high concentrations of oxygen vacancies in the nanorods and nanosheets. Obviously, the origins of the defects in the two types of nanostructures are different. In fact, the nanosheet morphology with large surfaces has high surface state densities and surface defects. However, in nanorods, an important factor for the existence of a strong peak of green emission is the presence of non-uniform Mg distribution in nanowires. The UV/DLE ratios for the nanorods and nanosheets are about 0.15 and 0.12 respectively. The small UV/DLE ratio obtained for the nanosheets is probably a result of their large area, where the surface effects dominate.

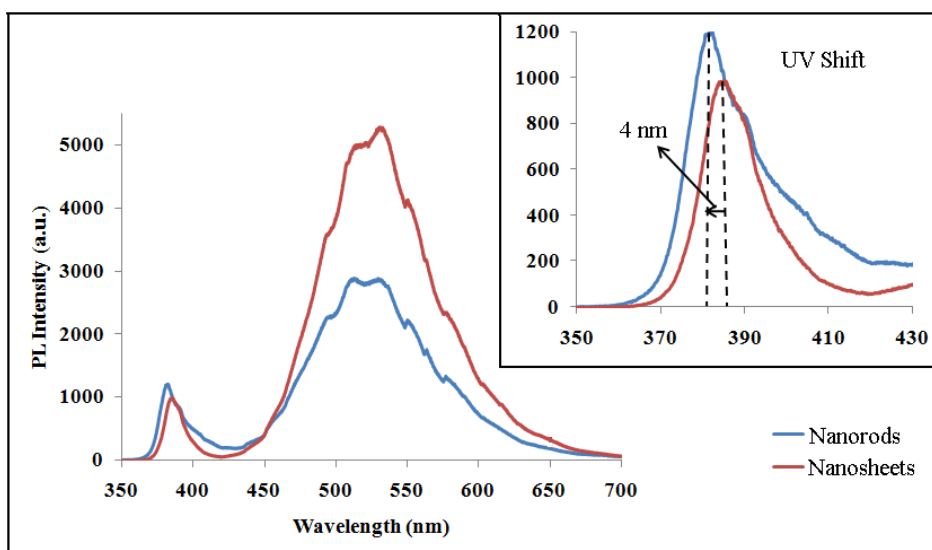


Figure 5.6. PL spectra of the ZnO nanorods and nanosheets. The inset shows that the UV peak of the nanorods grown at 700 °C is blue-shifted.

As shown in the inset in Fig. 5.6, the UV peak of the nanorods grown on the thin $Zn_{1-x}Mg_xO$ buffer layer is blue-shifted by 4 nm. This blue-shift comes from the modulation of the band-gap caused by the $Zn_{1-x}Mg_xO$ nanorods or the thin layer. Of course, a separation of these effects is very difficult to achieve. Note, that such a blue-shift cannot be due to the quantum confinement effect for the obtained nanorods, or surface effect that observed in previous chapter, since their average diameter is about 50 nm and since the quantum confinement effect does not occur in this range of diameters and also size of nanostructures in two samples is comparable.

One of the important factors in obtaining these results by thermal evaporation is the method of the source material preparation. A sintering method applied for preparing the source material causes ZnO and $Zn_xMg_{1-x}O$ to transform into corresponding vapors at approximately the same time. Our method can produce a thin layer of $Zn_{1-x}Mg_xO$ between the main substrate and the nanorods grown in the low temperature zone. Additionally, this method produce cubic $Zn_{1-x}Mg_xO$ nanorods with less Mg, and this is a main result of the sintering method preparation of the source material.

5.2.2. Growth of $Zn_{1-x}Mg_xO$ nanowires using a modified set-up

In the previous section observed that, gold catalyst had a significant role to doping of Mg in ZnO nanowires. Some researchers have reported that $Zn_{1-x}Mg_xO$ nanowires cannot be formed by the thermal evaporation method without using Au catalysts on Si substrates (Wang, F *et al.*, 2009; Zhi *et al.* 2005). We could not also obtain $Zn_{1-x}Mg_xO$ nanowires without the using of gold catalyst in our previous section. This may be due to smaller electronegativity difference between Mg and Si ($\zeta_{Si} - \zeta_{Mg} \approx 0.6$) in comparison to that between Mg and Au ($\zeta_{Au} - \zeta_{Mg} \approx 1.3$). A larger electronegativity difference creates a large electric field between the vapors and nuclei sites on substrate, which is needed to grow 1D nanostructure by such methods (Mohammad, 2008). Thus, finding a way to remove the gold catalyst after the growth process of $Zn_{1-x}Mg_xO$ nanowires may be important for recyclable use.

Based on these reasons, in this section Mg-doped ZnO nanowires are grown in the modified set-up. Additionally, the effects of the Au catalyst on the growth process of $Zn_{1-x}Mg_xO$ nanowires are investigated. The resultant $Zn_{1-x}Mg_xO$ nanowires obtained without the assistance of a gold catalyst. Moreover, the effects of different thicknesses of gold catalysts on the growth process of $Zn_{1-x}Mg_xO$ nanowires are investigated.

5.2.2.1 Experimental details

The growth of $Zn_{1-x}Mg_xO$ nanowires was performed in a horizontal furnace. The same method, which was used in previous chapter, is used to modify our set-up in this step. A mixture of the zinc oxide powder (99.99%) and commercial graphite powder at a 1:1 weight ratio was used as the precursor material of ZnO, and Mg powder (99.99%) was used as the precursor material of Mg ($Mol_{ZnO}/Mol_{Mg}=10:2$). The procure material of ZnO was placed at the closed end of the smaller quartz tube, while the Mg powder was placed 15 cm away from the ZnO material, and a Si(111) substrate was placed

downstream of the precursor materials, as shown in Fig. 5.7. The precursor materials of ZnO and Mg were heated up to 950 and 750°C respectively, and the temperature of the substrate was maintained at 600°C during the growth process of the $Zn_{1-x}Mg_xO$ nanowires (Fig. 5.7). The other conditions are the same with previous section. In this manner, three sets of wires made, one using a catalyst-free substrate (sample (a)) and the others using substrates coated with 10-nm (sample (b)) and 30-nm (sample (c)) Au films. Undoped ZnO nanowires were also grown under the same conditions using a catalyst-free substrate as sample (d) (from previous chapter).

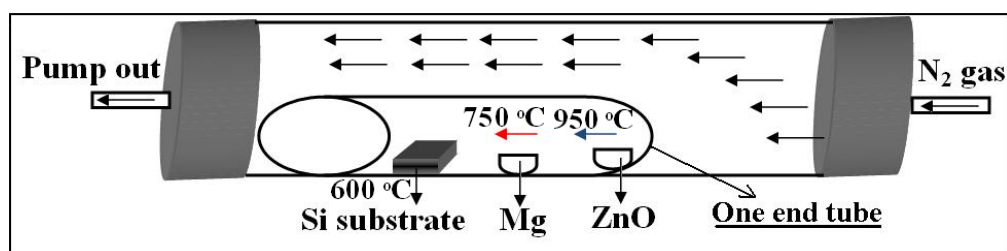


Figure. 5.7. Schematic of set-up that used for growth of $Zn_{1-x}Mg_xO$ nanowires.

5.2.2.2. Results and discussion

Figures 5.8(a₁-c₁) show low-magnification FESEM images of the $Zn_{1-x}Mg_xO$ nanowires that were grown on the various substrates: without a gold catalyst (sample (a)), with a 10-nm-thick gold film (sample (b)) and with a 30-nm-thick gold film (sample (c)), respectively. Figures 5.8(a₂-c₂) show high-magnification FESEM images and EDX spectra at different locations along individual $Zn_{1-x}Mg_xO$ nanowires, which were grown on the substrates under different conditions. As can be observed in the FESEM images, the shapes of these nanowires are dramatically different. Figure 5.8(a₂) shows a single $Zn_{1-x}Mg_xO$ nanowire with its EDX spectra taken from different places along this nanowire, which was grown on the catalyst-free substrate. A rectangular shape of this nanowire can be clearly seen in Fig. 5.8 (a₂). It can be seen that, the nanowire is not straight and that it does not have a uniform width for two of the sides

along its axis. In addition, the EDX spectra indicate an increase in the percent composition of Mg when moving towards the tip of the nanowire.

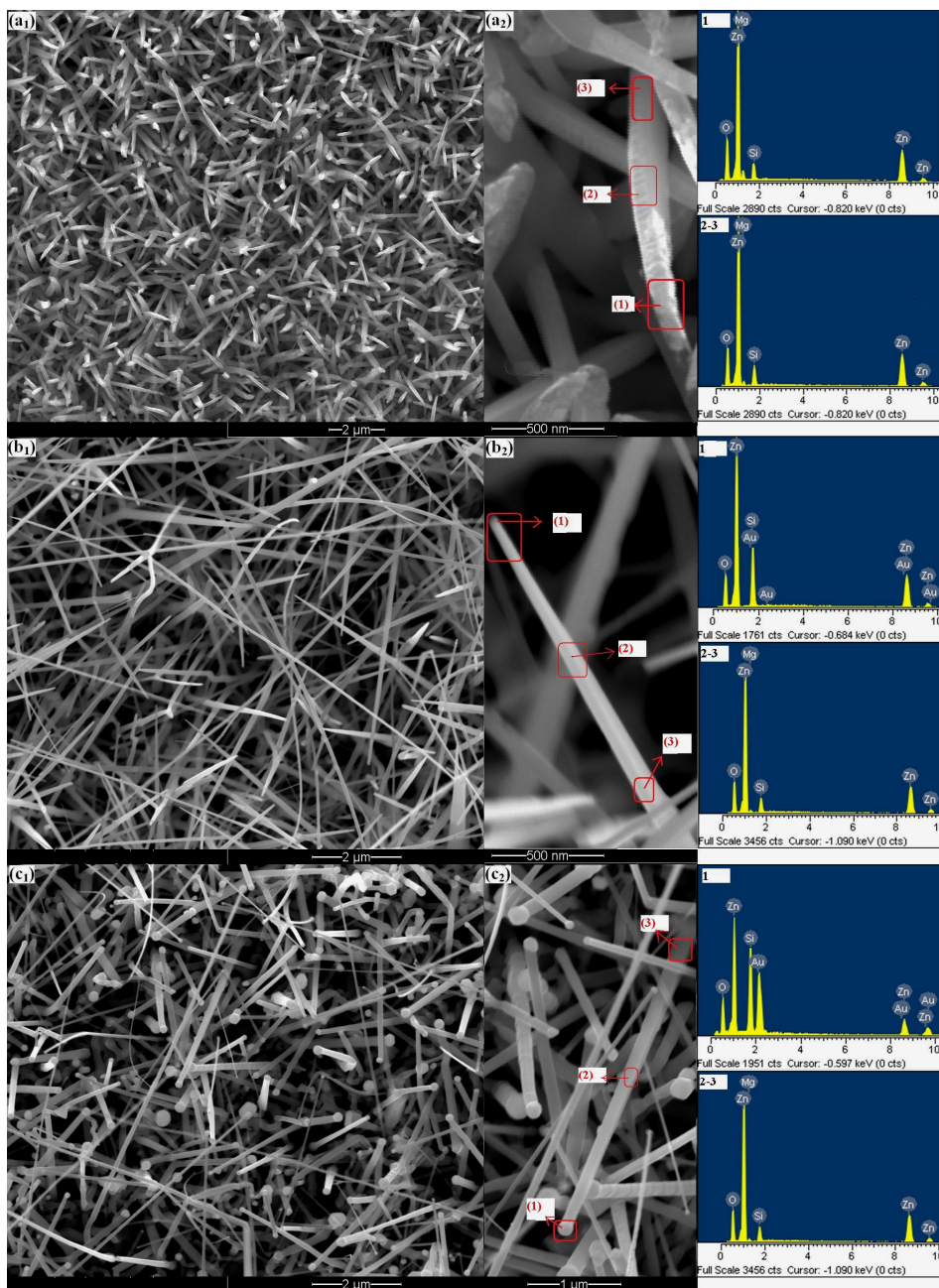


Figure. 5.8. Low-magnification FESEM images of the $Zn_{1-x}Mg_xO$ nanowires that were grown on the (a₁) catalyst-free substrate, (b₁) substrate coated with 10-nm-thick Au film, and (c₁) substrate coated with 30-nm-thick Au film. (a₂-c₂) High-magnification FESEM images of the $Zn_{1-x}Mg_xO$ nanowires with EDX spectra at different locations of along individual nanowire.

Figures 5.8(b₂) and (c₂) also show individual Zn_{1-x}Mg_xO nanowires with their EDX spectra taken from different places along these nanowires, which were grown on the substrates coated with 10- (sample (b)) and 30-nm (sample (c)) Au films, respectively. The shapes of these nanowires are completely different in comparison to the nanowires that were grown on the catalyst-free substrate. As is visible in the FESEM images, the nanowires are completely straight, but are tapered with tip diameters of 10 ± 2 and 80 ± 5 nm and base diameters of 80 ± 5 and 130 ± 10 nm for samples (b) and (c), respectively. By a comparison observation between Zn_{1-x}Mg_xO nanowires, it can be understood that tapering of the Zn_{1-x}Mg_xO nanowires may be due to the reaction product. In fact, the disturbance of the vapor concentration in growth process of Zn_{1-x}Mg_xO nanowires is a major factor that changes the diameter of the catalyst alloy droplets. Moreover, stability of catalyst alloy droplets during of the growth process is dependent on eutectic temperature of compounds in alloy droplet (Mohammad, 2008). Therefore, existence of Mg may be changed Au-Zn eutectic temperature during the growth process, because concentration of Mg will be changed by prolonging of growth time. The diameter of the nanowires grown with the 30-nm-thick gold film is larger than the diameter of the nanowires grown with the 10-nm-thick gold film, because the nanowire diameter is known to be dependent on catalyst particle size. The thicker gold film produces larger gold droplets, so the nanowires grown with the thicker gold film have a larger diameter. Based on the results obtained from the EDX spectra of these nanowires, the growth process of these nanowires is determined to be the VLS process. One can clearly observe gold particles at the tips of the nanowires in Fig. 5.8 (c₁) and 5.8 (c₂). The Mg element is not detected at the nanowire tips that were grown on the substrates coated with Au.

Table 5.1 shows the average Mg content in the $Zn_{1-x}Mg_xO$ nanowires. It can be clearly observed that the $Zn_{1-x}Mg_xO$ nanowires were grown on the catalyst-free substrate have more content of Mg than the other $Zn_{1-x}Mg_xO$ nanowires.

Table 5.1. Average Mg content in the $Zn_{1-x}Mg_xO$ nanowires grown on the various substrates and the Mg content at different locations of a single nanowire.

Positions at the single nanowire	The tip	The middle	The bottom	Average of Mg at%
Sample a (without Au): Mg (at %)	8.4%	4.3%	3.1%	5.2%
Sample b (with 10 nm Au): Mg (at %)	0	3.8%	3.0%	2.5%
Sample c (with 30 nm Au): Mg (at %)	0	3.5%	3.2%	2.4%

Additionally, this table shows the Mg content at different positions of a single nanowire for three samples: 1) of the tip, 2) of the middle and 3) of the bottom. According to this table, samples (b) and (c) show that the Mg content and distribution of Mg are not affected by the increased gold film thickness.

The undoped ZnO nanowires that were grown with the same conditions in previous chapter is selected as a comparative sample (sample (d)) with these Mg-doped samples (Fig. 5.9). Unlike the $Zn_{1-x}Mg_xO$ nanowires, the undoped ZnO nanowires are not tapered, and they possess a uniform diameter of about 90 nm on average. In addition, it can be observed that the undoped ZnO nanowires have a hexagonal face at the tip and the majority of them are perpendicular to the substrate. In fact, the growth direction of the undoped ZnO nanowires is along the c-axis.

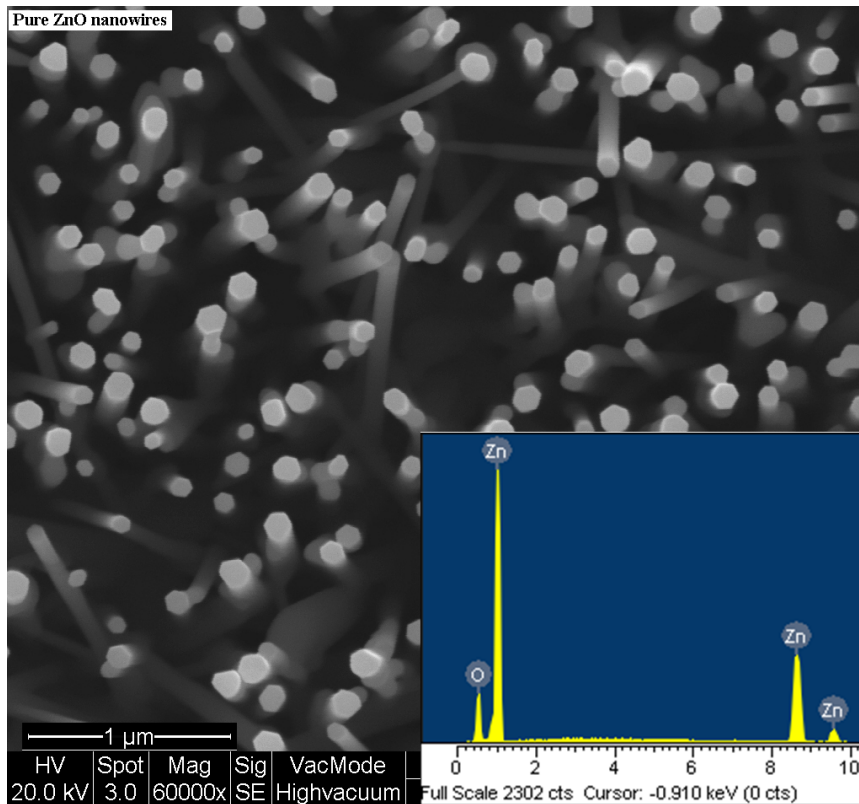


Figure. 5.9. FESEM image and EDX spectrum of the undoped ZnO nanowires that grown on the catalyst-free substrate.

The growth mechanism of $Zn_{1-x}Mg_xO$ nanowires can also be tentatively proposed by Fick's law. Based on these reasons, Mg and ZnO vapors can propagate toward the substrate in our configuration (Fig. 5.7), but the Mg vapors reach the substrate sooner than the ZnO vapors, due to the lower melting point of Mg in comparison to ZnO as well as the fact that the Mg boat is closer to the substrate than the ZnO boat. When the Mg vapors reach the substrate that is placed at 600 °C, they condense and form ideal nucleation sites for the absorption of ZnO vapors on the catalyst-free Si substrate. In fact, Mg droplets could act in a self-catalyst role for the growth of $Zn_{1-x}Mg_xO$ nanowires (Fig. 5.10 a). Therefore, the growth of the $Zn_{1-x}Mg_xO$ nanowires grown on the catalyst-free substrate could also be controlled by the VLS mechanism. Thereby, the vapors of ZnO_x were absorbed by the self-catalyst, reached saturation and then were finally solidified.

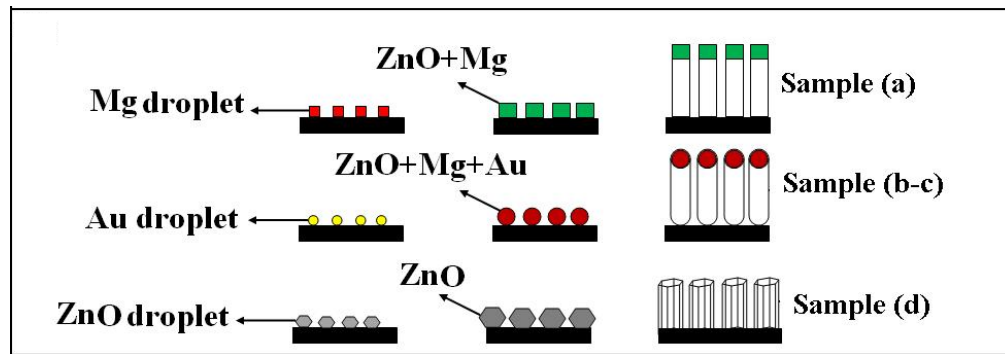


Figure. 5.10. Schematic of $Zn_{1-x}Mg_xO$ and ZnO nanowires formation on various substrates.

Additionally, the change in the diameter of the nanowires during growth is due to the change in the droplet size of the self-catalyst. In fact, during the growth process, the Mg catalyst diffuses into the nanowires. Since the nanowire diameter size is determined by the catalyst size within the framework of the VLS mechanism, such catalyst diffusion causes a change in the nanowire diameter. This behavior can be supported by the changing Mg content along the nanowire axis (Table 5.1, sample (a)). Such a mechanism can act in the growth of the other samples ((b-c)), which were grown with a gold catalyst.

The only difference between these samples is the initial droplets. In addition, this theory may be supported by the different shapes of these nanowires, because it is known that the shape of a nanowire is dependent on its initial site: 1) sample (a), the nanowires have a cubic shape according to the cubic structures of Mg (Fig. 5.10 (a)); 2) samples (b) and (c), the nanowires have followed the spherical shape of the gold sites (Fig. 5.10 (b-c)). It can be seen that the pure ZnO nanowires have a uniform diameter along their c-axis and that no catalyst particles are detected on the undoped ZnO nanowire tips (Fig. 5.10 (d)). A comparison between these four samples shows that the catalyst has a significant role in the formation of the different shapes.

Two key questions here are: 1) If a large electronegativity difference is necessary for the formation of the $Zn_{1-x}Mg_xO$ nanowires (Mohammad, 2008), how is Mg doped without using the gold catalyst in the case of the catalyst-free substrate? 2) Why is the Mg content in the $Zn_{1-x}Mg_xO$ nanowires grown on the catalyst-free substrate more than that of the other $Zn_{1-x}Mg_xO$ nanowires? Based on our previous section and other reports of Mg doping in ZnO, no $Zn_{1-x}Mg_xO$ nanowires have been formed by the thermal evaporation method without using Au catalysts. In fact, when the Mg is used as a doping material in a conventional furnace tube (open tube), the concentration of Mg in the atmosphere of the tube is very low. Therefore, in this condition, the electronegativity difference between the vapor particles and substrate can be important. On the other hand, if the concentration of the Mg in the furnace is increased, then the electronegativity difference is not an important factor, because the high concentration of Mg in this set-up may adjust for the small electronegativity difference. Thus, the modified thermal evaporation set-up caused the concentration of Mg as an impurity in the tube to increase and Mg was doped in the ZnO without using Au. Mg droplets at the tip of the nanowires can also absorb a greater amount of Mg vapor in comparison to a gold droplet.

Figure 5.11 shows XRD patterns for the $Zn_{1-x}Mg_xO$ (a-c) and undoped ZnO (d) nanowires. The XRD patterns in Fig. 5.11 agree with the standard card of bulk ZnO with a hexagonal structure. No peaks from Zn, Mg or other impurities are visible, except for sample (c), which shows an additional peak that corresponds to the Au(111) catalyst. The peak of Au appears in sample (c) because all nanowires in this sample have gold caps on their tips. Doping with Mg causes a slight shift of the (002) XRD peaks toward higher diffraction angles. The extent of these shifts is dependent on the Mg content in the nanowires. Therefore, the (002) peak of sample (a) exhibits a larger

shift in comparison to that of the other nanowires. These shifts are shown in the inset of Fig. 5.11.

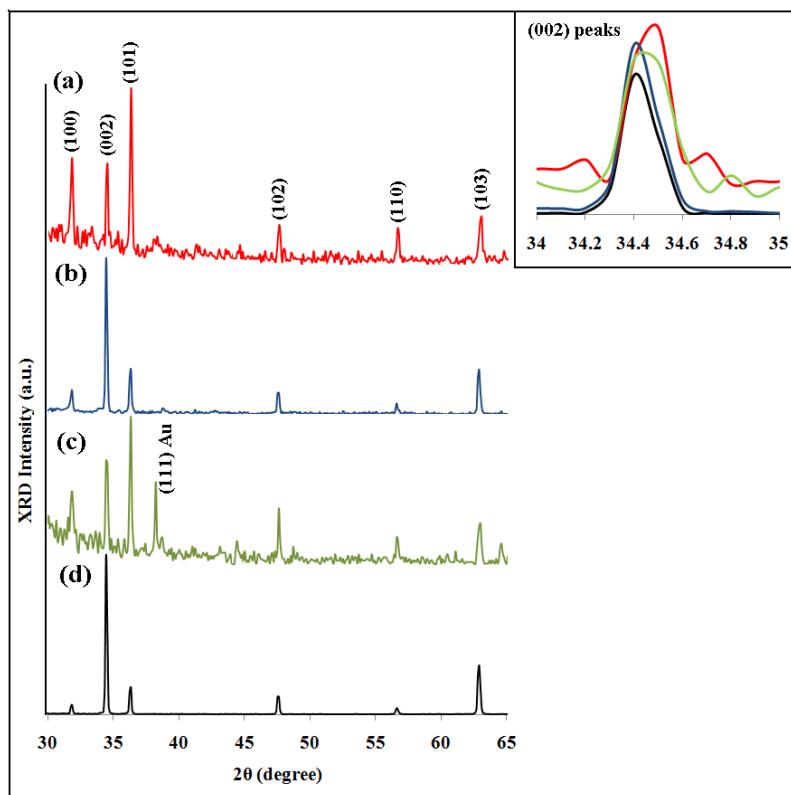


Figure. 5.11. XRD patterns of the $Zn_{1-x}Mg_xO$ nanowires grown on the (a) catalyst-free substrate, (b) substrate coated with 10-nm-thick Au film, (c) substrate coated with 30-nm-thick Au film, and (d) undoped ZnO nanowires. No peaks from impurities are detected, except for sample (c), which shows an additional peak that corresponds to the Au(111) catalyst. The inset shows the shifts of (002) peaks of the $Zn_{1-x}Mg_xO$ nanowires in comparison to the (002) peak of the undoped ZnO nanowires.

Figure 5.12 shows the room temperature PL spectra of the $Zn_{1-x}Mg_xO$ (a-c) and undoped ZnO (d) nanowires. All of the PL spectra show a strong peak in the UV region and negligible green emission, except for sample (c), which shows a slightly stronger green emission peak in comparison to the other nanowires. Compared with the undoped ZnO nanowires (sample (d)), all of the $Zn_{1-x}Mg_xO$ samples show an obvious blue-shift in the UV emission. Particularly, for sample (a), which has a higher Mg content than the other $Zn_{1-x}Mg_xO$ nanowires, the UV emission is blue-shifted to 361 nm from 384 nm,

due to the modulation of the band-gap caused by Mg substitution. The blue-shift in the UV emission is believed to be a result of the band-gap engineering by Mg.

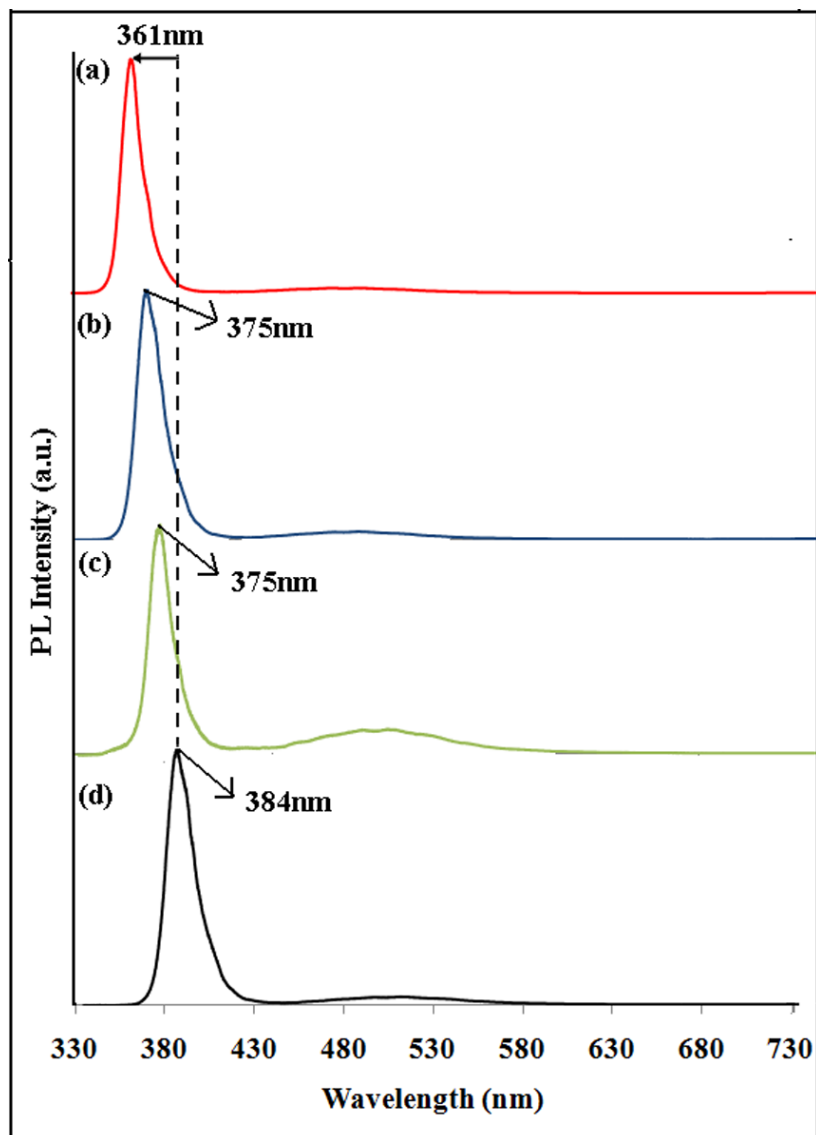


Figure. 5.12. PL spectra of the $Zn_{1-x}Mg_xO$ nanowires grown on the (a) catalyst-free substrate, (b) substrate coated with 10-nm-thick Au film, (c) substrate coated with 30-nm-thick Au film, and (d) undoped ZnO nanowires. All of the $Zn_{1-x}Mg_xO$ samples show an obvious blue-shift in the UV emission in comparison to the undoped ZnO nanowires.

As the concentration of Mg increases, the blue-shift of the UV peak also increases. This result has a significant agreement with theoretically results in Chapter Two. These results in comparison to our previous results in the previous section show greater optical efficiency.

Raman spectra of the $Zn_{1-x}Mg_xO$ (samples (a-c)) and undoped ZnO (sample (d)) nanowires are presented in Fig. 5.13.

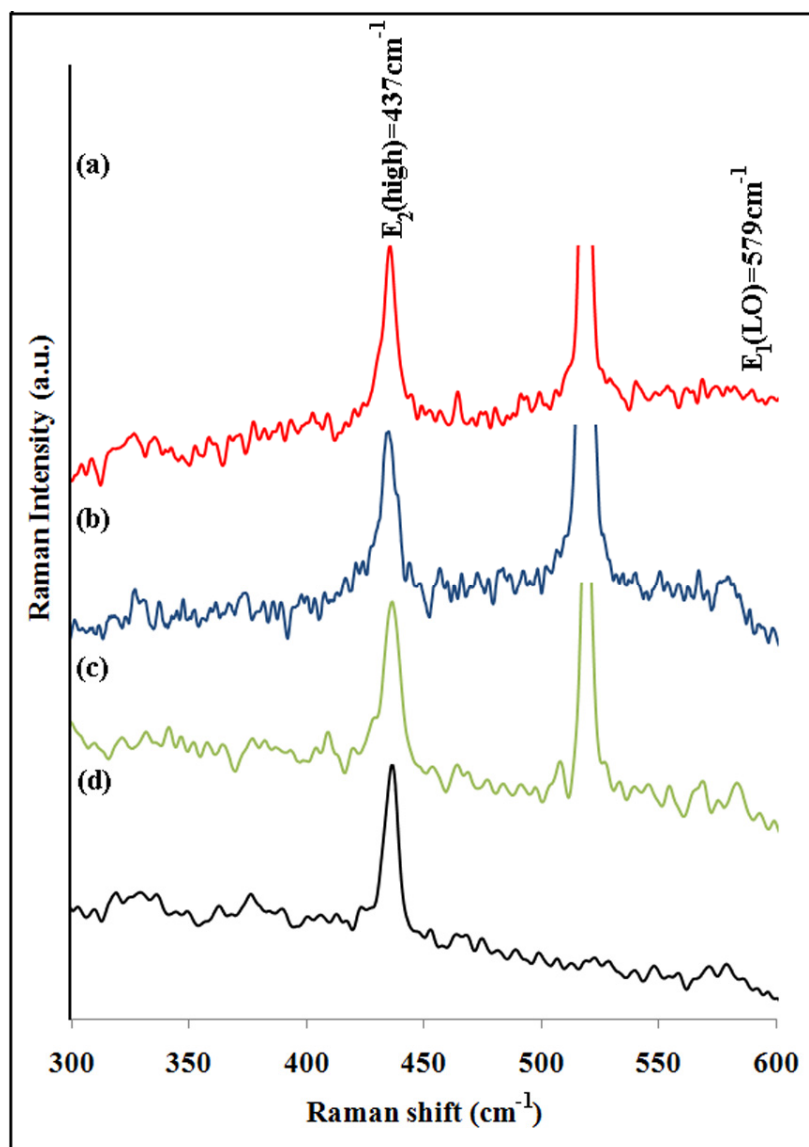


Figure 5.13. Raman spectra of the $Zn_{1-x}Mg_xO$ nanowires grown on the (a) catalyst-free substrate, (b) substrate coated with 10-nm-thick Au film, (c) substrate coated with 30-nm-thick Au film, and (d) undoped ZnO nanowires. All of the nanowires show a sharp, strong and dominant peak at 437 cm^{-1} corresponding to the $E_2(\text{high})$ mode of the Raman active mode.

As shown in Fig. 5.13, the Raman spectra of all of the nanowires show a sharp, strong, and dominant peak at 437 cm^{-1} corresponding to the $E_2(\text{high})$ mode of the Raman active mode. A weak peak at 579 cm^{-1} corresponding to $E_1(\text{LO})$ is indicated for the $Zn_{1-x}Mg_xO$ nanowires that were grown on the substrates coated with Au. Therefore, the appearance

of the $E_1(\text{LO})$ mode for samples (b) and (c) indicates a lower crystalline quality and higher oxygen vacancy of the $\text{Zn}_{1-x}\text{Mg}_x\text{O}$ nanowires grown on the substrates coated with Au films in comparison to the $\text{Zn}_{1-x}\text{Mg}_x\text{O}$ and undoped ZnO nanowires grown on the catalyst-free substrates. Therefore, the existence of a catalyst such as Au in the nanowire tips may cause the decreased crystalline quality of the ZnO nanowires. In fact, the Raman results have a good agreement with the PL results.

5.2.3. Field emission study of $\text{Zn}_{1-x}\text{Mg}_x\text{O}$ nanowires

It is known, one of the most important factors in field emission study is nanowires shape. Therefore, in previous section was seen that, thickness of gold catalyst affected shape of $\text{Zn}_{1-x}\text{Mg}_x\text{O}$ nanowires that were grown by VLS method (sample (b) and (c) that their names are changed sample (a) and (b), respectively in this section). In fact, tapering of the nanowires can be a good factor for field emission studies. Therefore, in this section effect of different morphology of $\text{Zn}_{1-x}\text{Mg}_x\text{O}$ nanowires on field emission properties is presented. In addition, a few studies reported about field emission of $\text{Zn}_{1-x}\text{Mg}_x\text{O}$ nanostructures (Pan *et al.*, 2006).

The field emission current density-applied field (J - E) characteristic of the $\text{Zn}_{1-x}\text{Mg}_x\text{O}/\text{Au}(10\text{nm})$ (sample (a)) and $\text{Zn}_{1-x}\text{Mg}_x\text{O}/\text{Au}(30\text{nm})$ (sample (b)) nanowires is shown in Fig. 5.14 (a). The turn-on field corresponding to emission current density of $10 \mu\text{A}/\text{cm}^2$ is found to be $0.78 \text{ V}/\mu\text{m}$ and $1.62 \text{ V}/\mu\text{m}$ for the samples (a) and (b), respectively. It is well-known that there are several factors which can be affected the value of turn-on field, such as aspect ratio, tip radius, crystal structure, conductivity, work function, and nanostructure density. A careful observation of surface morphology, it is clear that the areal density of nanowires in case of ZnMgO/Au (10nm) is higher than ZnMgO/Au (30nm) (Fig 5.8). It is expected that the combination of higher density of the emitters along with radius

of tip should be the main factors to reduce the turn-on field of the ZnMgO/Au (10nm) nanowires. For the sake of comparison with other results reported in the literature, the threshold field, required to draw emission current density $\sim 100 \mu\text{A}/\text{cm}^2$, is observed to be 1.22 V/ μm and 2.32 V/ μm for the samples (a) and (b), respectively. The observed values of threshold field are superior to those reported for various ZnO nanostructures (Sheini *et al.*, 2009; Zhao *et al.*, 2006; Wei *et al.*, 2006). The lowest value of observed threshold field for the sample (a) is attributed to their higher aspect ratio as compared to the sample (b).

The F-N plot, i.e. $\ln(J/E^2)$ versus $(1/E)$, derived from the observed J - E characteristic is shown in Fig. 5.14 (b). It is clear that the measured data fit well with the F-N equation (Equation (2-11)):

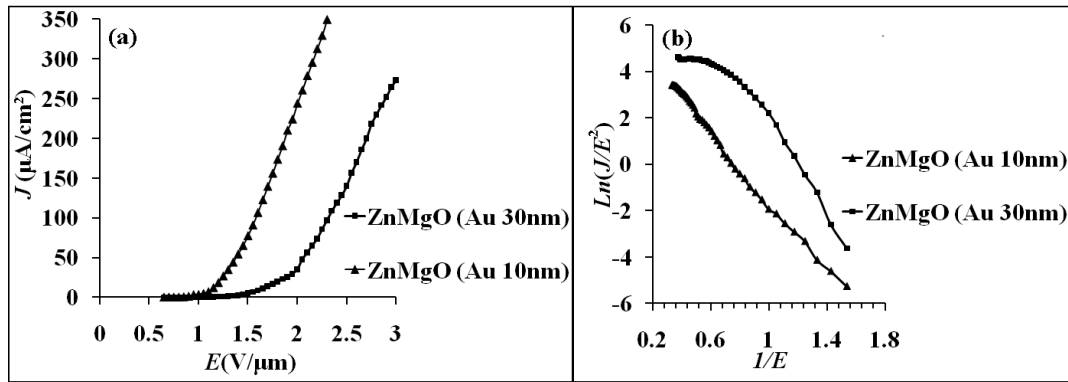


Figure. 5.14. (a) J - E plots of the field emission from the $\text{Zn}_{1-x}\text{Mg}_x\text{O}$ nanowires grown on the substrate coated with 10-nm-thick Au film (sample (a)) and substrate coated with 30-nm-thick Au film (sample (b)). (b) F-N plots of the field emission from these nanowires.

The calculated field enhancement factor β from the slope of F-N curves in Fig. 5.14 (b) is 2310 and 1140 for the samples (a) and (b), respectively. This significant difference between β values of samples can be attributed to sharper tip and better crystallinity quality of the sample (a) than the sample (b) according to FESEM, PL, and Raman results. The value of β factor is higher than those reported in the literature for well aligned ZnO nanowires (Li, C *et al.*, 2007), nanonails and nanopencils (Shen *et al.*, 2006), nanocones (Bae, *et al.*, 2009), nanotips (Cheng, C.L. *et al.*, 2009), and $\text{Zn}_{1-x}\text{Mg}_x\text{O}$ tetrapods (Pan *et*

al., 2006), although our nanowires were randomly oriented. In fact, not only the Mg doping may enhance the conductivity of ZnO but also tapering of the $Zn_{1-x}Mg_xO$ nanowires may increase field emission property of $Zn_{1-x}Mg_xO$ nanowires.

The emission current stability of the samples (a) and (b) has been investigated at the pre-set current value of 10 μA over the duration of three hours. The corresponding emission current-time (I-t) plots recorded at the base pressure of 1×10^{-8} mbar are shown in Fig. 5.15. As seen from Fig. 5.15, for the sample (a) show good stability at the pre-set current value. In case of the sample (b) as emitter, the emission current initially increases and then stabilizes to a higher value $\sim 14 \mu A$. At the “stabilized value”, the overall current stability is observed to be fairly good. The observed increase in the emission current followed by stabilization indicative of ‘conditioning’ of the emitter surface during continuous emission studies.

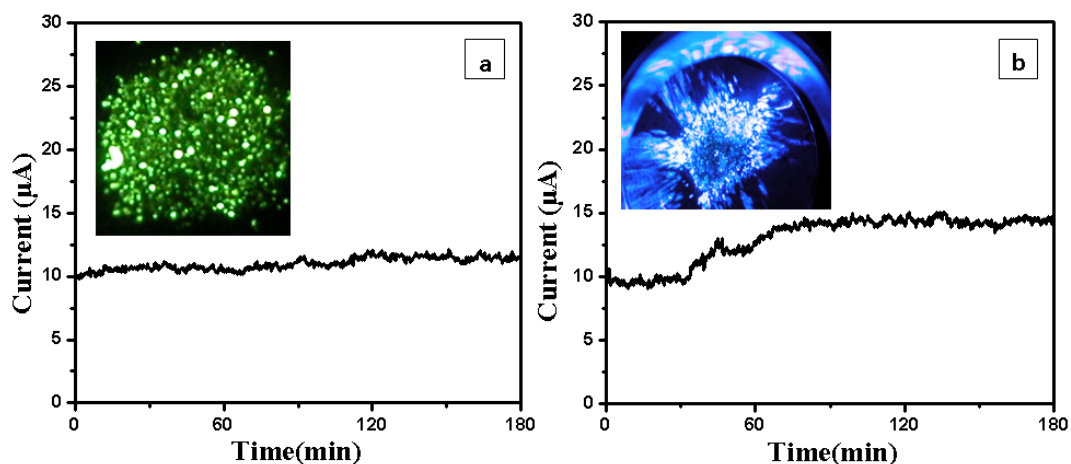


Figure. 5.15. I-t plots recorded of the $Zn_{1-x}Mg_xO$ nanowires grown on the: (a) substrate coated with 10-nm-thick Au film (sample (a)), and (b) substrate coated with 30-nm-thick Au film (sample (b)). The insets are the corresponding luminescence images of the nanowires.

The emission current initially exhibits excursions from the average value along with some superimposed ‘spike’-type fluctuations, subsequently stabilizing with reduced fluctuations. The ‘spike’-type fluctuations are due to the adsorption, desorption, and/or migration of the residual gas molecules on the emitter surface. The variations in the

emission current can be understood by the role played by the residual gas ion bombardment during the continuous operation of the emitter. There are various processes occurring simultaneously on the emitter surface which affect the emission current. A residual atom adsorbed on the emitter surface may cause resonance tunneling thereby increasing the emission current and its desorption due to ion bombardment leading to a reduction in the emission current. In addition, an initial ion bombardment induced cleaning of the emitter surface helps in stabilizing the emission current. On the other hand, the ion bombardment induced sputtering of the emitting site may cause a decrease in the emission current. As we have used as-synthesized specimens for field emission studies, it is expected that the emitter surface is “not clean” and also no cleaning attempt such as degassing by heating the emitter has been carried out, the trend in the observed $I-t$ curve is indicative of the ion bombardment induced cleaning of the emitter surface. The results suggest that the sample (a) as emitter is a potentially important system for applications in field emission based devices. A post FESEM study indicated no significant change in the overall surface morphology of both the samples (a) and (b) emphasizing that the two emitters are mechanically very robust against the stresses due to the intense applied electric field and ion bombardment. A typical field emission image, captured at current value of 10 μA is shown as in the insets of Fig. 5.15. The image shows a number of tiny spots, which correspond to emission from the most protruding ZnMgO/Au(10nm) nanowires (sample (a)). Temporal changes in the image spots intensity have been observed to be commensurate with the emission current fluctuation as seen in $I-t$ plot.

5.3. Al-doped ZnO nanowires using AlN thin films

In this section, we present the synthesis and characterization of high-aspect-ratio ZnO nanowires on the AlN thin film deposited on the glass substrate using thermal evaporation method at different substrate temperatures in a conventional tube furnace. It will be observed that the AlN thin film will play as a doping source role during the growth of ZnO nanowires. In fact, one of the best places for doping source in thermal evaporation method is on substrate (Yong *et al.*, 2009).

5.3.1. Experimental details

First of all, the glass substrates were ultrasonically cleaned in acetone, methanol, and de-ionized water for about 30 min. Then, the AlN films were deposited on the glass substrates by a direct-current (DC) cylindrical magnetron sputtering system from a high purity aluminum target in an argon (99.99%) and nitrogen (99.99%) gas mixture. The target to substrates distance was about 30 cm. The glass substrate temperatures were held at 300 °C during AlN deposition process. Therefore, the AlN thin film with about 15-20 nm thickness was obtained. All conditions for growth of the ZnO nanowire on the AlN thin films are similar to section 5.1 except for substrate places, which have placed at 500 and 600 °C.

5.3.2. Results and discussion

Figure 5.16 shows XRD pattern of AlN thin film that is deposited on glass substrate. The XRD pattern in Fig. 5.16 agrees with the standard card of bulk AlN with cubic structure (JCPDS No. 461200). It is known that AlN has two structures, one hexagonal and another cubic. Existence of any structure depends on growth experimental conditions. Therefore, we could obtain AlN thin film with cubic structures with these conditions.

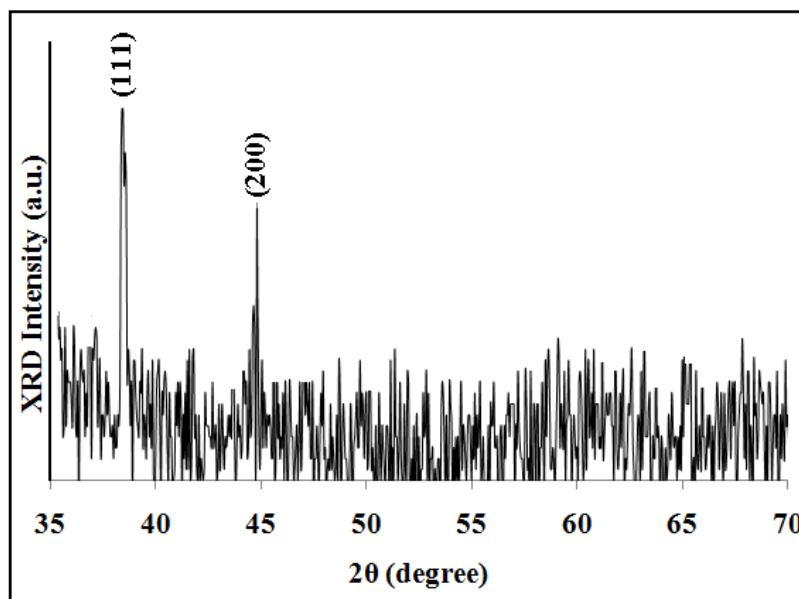


Figure 5.16. XRD pattern of AlN thin film with cubic structure deposited on glass.

Figures 5.17 (a-b) show the FESEM images and the EDX spectra of some ZnO nanowires deposited at different substrate temperatures (similar the previous results).

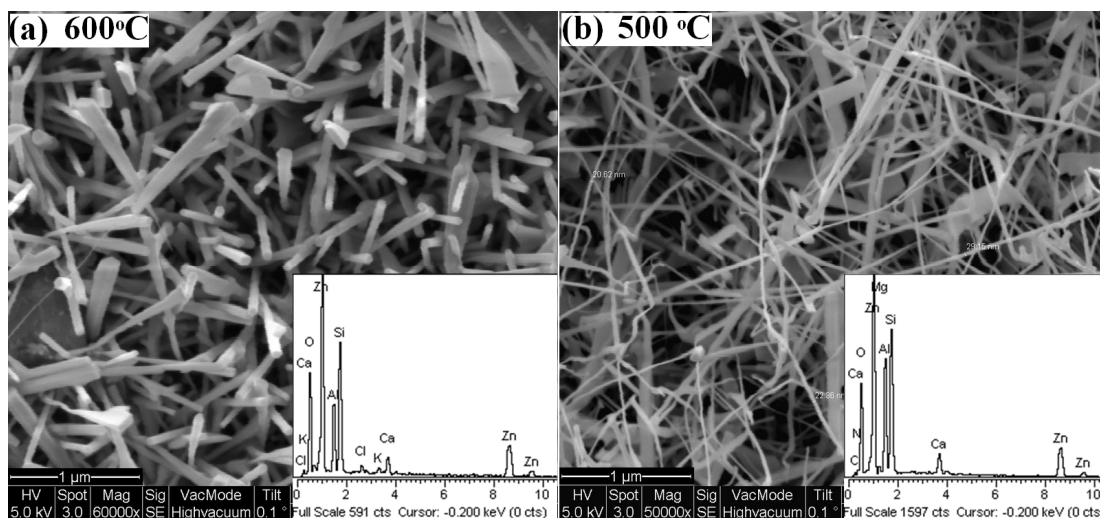


Figure 5.17. FESEM images and EDX spectra of the ZnO nanowires grown on the AlN thin film at (a) 600 °C and (b) 500 °C. The shapes of the ZnO nanowires are varied with the distance from the source material to the substrates.

The shape of ZnO nanowires was formed to vary with the distance from the source material to the substrates. The nanowires grown at 600 °C are straight, semi-perpendicular to substrate and have hexagonal shaped tips. The typical average

diameters of the nanowires grown at 600 and 500 °C were about 57 and 22 nm respectively, with several micrometers in length. The EDX measurements show the strong signals from zinc, oxygen, the signals from the AlN thin film, and components of the glass substrates were detected.

Figures 5.18 (a-b) show XRD patterns of nanostructures grown on substrates at 600 and 500 °C, respectively. The XRD patterns in Fig. 5.18 agree with the standard card of bulk ZnO with hexagonal structure. At 600 °C, the XRD pattern of the sample not only shows ZnO peaks but also presents three other peaks at 38.45°, 44.65° and 48.80°, which belong to ZnAlO composite. Such peaks show clearly that Al is diffused from the AlN thin film into the ZnO nanowires grown at 600 °C.

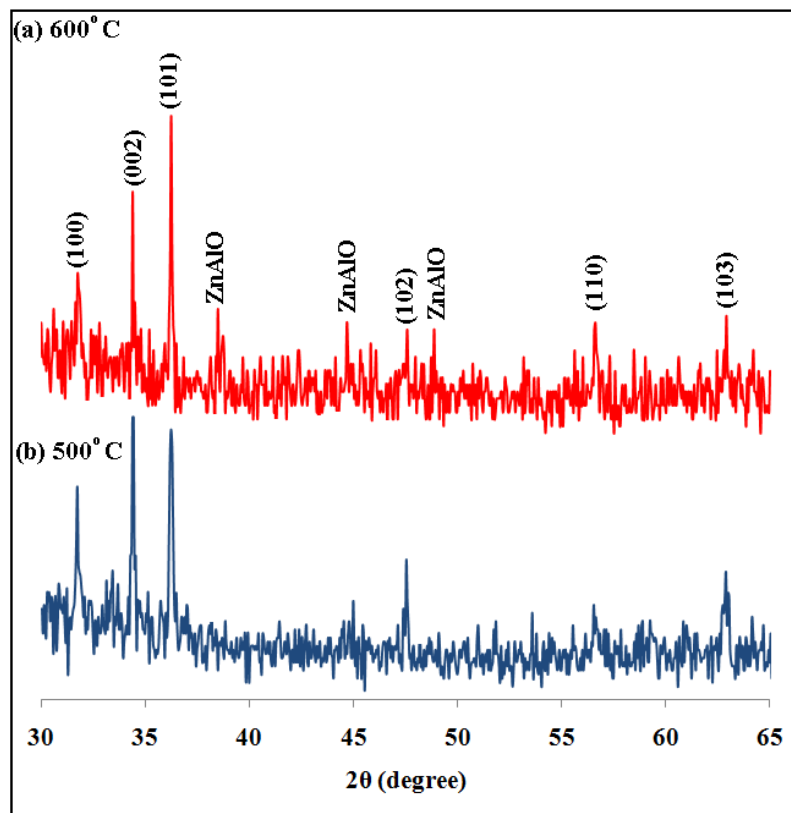


Figure 5.18. XRD patterns of the ZnO nanowires deposited at (a) 600 °C and (b) 500 °C. XRD pattern of the nanowires grown at 600 °C not only shows ZnO peaks but also presents three peaks at 38.45°, 44.65° and 48.80° which belong to ZnAlO composite.

Figures 5.19 (a-c) show high resolution N (E) Auger electron spectroscopy (AES) of oxygen, zinc, and aluminum, respectively, for the ZnO nanowires. The AES spectra of oxygen (Fig. 5.19 (a)) indicate clear peaks at 484 and 504 eV (500 °C), also 496 and 518 eV (600 °C) corresponding to the KLL Auger electron emission from oxygen. Figure 6.19 (b) shows spectra of zinc that indicate peaks at 817, 896, 909, 983 and 1004 eV (500 °C), also 828, 907, 921, 996 and 1010 eV (600 °C) corresponding to the LMM Auger electron emission of zinc. Figures 5.19 (a-b) show clearly a significant shift to higher energies for oxygen and zinc peaks for the nanowires grown at 600 °C. Figure 5.19 (c) shows spectra of aluminum that indicate a weak peak at 1340 eV and a strong peak at 1393 eV corresponding to the KLL Auger electron emission of Al for the sample grown at 600 °C. Aluminum Auger electron emission was not detected for the sample grown at 500 °C. In fact, diffusion of Al into the nanowires deposited in the high temperature zone cause that energy of Auger electron emission of zinc and oxygen shift to higher energies.

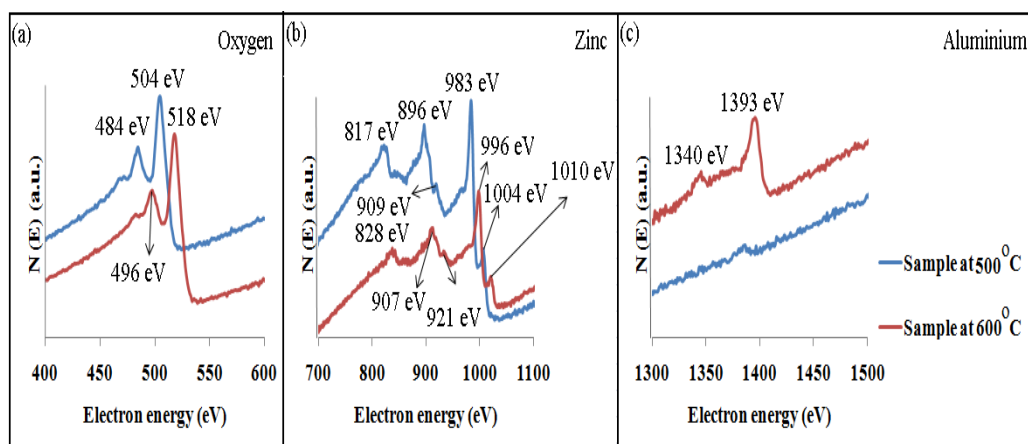


Figure 5.19. High resolution N (E) Auger electron emission spectroscopy of the ZnO nanowires deposited on the AlN thin film at 600 and 500 °C. (a) O spectra and (b) Zn spectra. These spectra show clearly a significant shift to higher energies for oxygen and zinc peaks for nanowires grown at 600 °C and also (c) Al spectra that show Al peaks only for the sample grown at 600 °C.

$$\begin{array}{l}
 \text{O(KLL)} \left\{ \begin{array}{l} 484 \text{ eV} \rightarrow 496 \text{ eV} \\ 504 \text{ eV} \rightarrow 518 \text{ eV} \end{array} \right. \\
 \text{Zn(LMM)} \left\{ \begin{array}{l} 817 \text{ eV} \rightarrow 828 \text{ eV} \\ 896 \text{ eV} \rightarrow 907 \text{ eV} \\ 909 \text{ eV} \rightarrow 921 \text{ eV} \\ 983 \text{ eV} \rightarrow 996 \text{ eV} \\ 1004 \text{ eV} \rightarrow 1010 \text{ eV} \end{array} \right. \quad (5-2)
 \end{array}$$

Because Al is a good conductor element, therefore it can increase amount of electrons density of ZnO and consequently causes of change Auger electrons energies of ZnO. Additionally, we compare these results with our previous nanowires that have the same diameter with the nanowires grown at 600 °C approximately (Fig. 5.20). It does not observe any shifts in Auger's peaks. Thus, such shifts of Auger electron energies cannot be due to different diameter of nanowires, thereby Al is the unique factor for the shift of Auger electron energies in the nanowires grown at 600 °C.

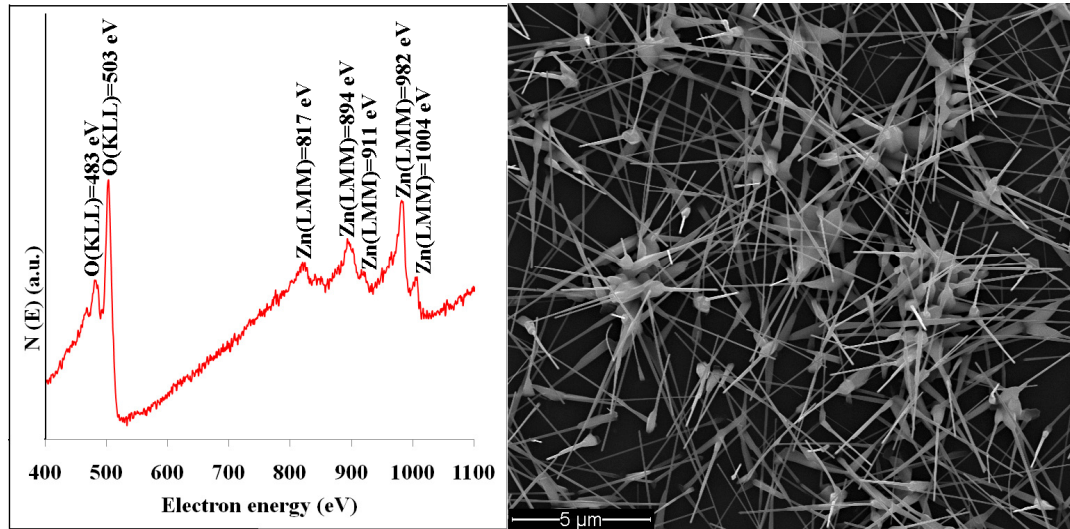


Figure 5.20. Auger spectrum and FESEM image of ZnO nanowires grown on Si substrate that average diameter of these nanowires is about 60 nm.

The XRD and AES show the diffusion of Al into the nanowires grown in the high temperature zone. Probable explanation could be the diffusion of Al from the AlN thin film into the ZnO nanowires grown at 600 °C. The melting point of bulk AlN is 2200 °C at atmosphere pressure condition, but AlN thin film at 800 Pa and 600 °C has enough energy to transform into a cluster form. Thus, Al has diffused into the ZnO nanowires grown at 600 °C.

PL measurements were performed to study the optical properties of the ZnO nanowires. Also, two emission bands appeared in the all PL spectra of ZnO nanowires, one related to the UV emission at 380-382nm, and the other related to the DLE at 503-505nm. Figure 5.21 shows the PL spectra of deposited ZnO nanowires. As shown in the inset in Fig. 5.21, the UV peak of the nanowires grown at 500 °C is blue shifted by about 2 nm. The results obtained from the FESEM images show that the ZnO nanowires grown at 500 °C have smaller diameters than those grown at 600 °C. In fact, this result can confirm the results obtained in the previous section about the size effect on the optical properties of ZnO nanowires. Burstein-Moss effect for the nanowires, which are doped with Al, is not probably observed in the nanowires due to low concentration of Al in these nanowires. The UV/DLE ratio for the nanowires grown at 600 and 500 °C is about 1.97 and 2.65 respectively. The small UV/DLE ratio for the nanowires grown at 600 °C is probably due to existence of Al in the nanowires. The ZnO nanowires grown at 600 °C exhibit a higher concentration of oxygen vacancies because of site competition between Al and Zn atoms. This implies that a high intensity of the green emission band was obtained in the ZnO nanowires grown at 600 °C as compared to those grown at 500 °C.

In fact, the ZnO nanowires with Al, exhibit a higher concentration of defects such stacking faults that due to big difference in the ionic radii of Al³⁺ (0.051 nm) and Zn²⁺ (0.074 nm). Therefore, Al³⁺ easily substitutes Zn²⁺ at a lower doping concentration and the introduction of Al-ions into the lattices of ZnO leads the large structural strain which causes the origination of the stacking faults in the ZnO nanowires. This defect is not only essential for the growth of the ZnO nanostructures, but also strongly affects their optical, electrical, and possibly chemical properties (Ding & Wang, 2009). In addition, Hur *et al.* (2004) proposed that Al-impurity could be affected the green emission band in indirect recombination path. Because the contribution of the green

band emission in undoped ZnO is only from the intrinsic delocalized conducting states or partially localized impurity states which was called “effective band”. Thermally excited electrons of Al-impurity level become transferred to the conducting state.

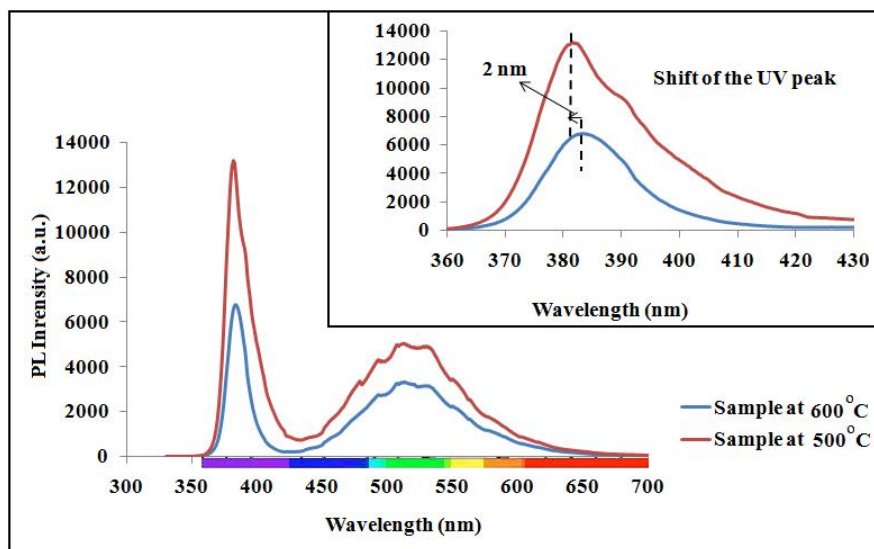


Figure 5.21. PL spectra of the ZnO nanowires deposited at 600 and 500 °C. The inset shows the UV peak of nanowires grown in the low temperature zone is blue shifted, because the diameters of nanowires in this zone are smaller than those grown in the high temperature zone.

The electron charge transfer is carried out from the localized impurity state to the effective band by the potential fluctuation of the Al-impurity band in the excitation process. The charge transfer to the effective band is dominated by the Al-impurity state which has low localization energy. We also observe that intensity of the green emission for the ZnO nanowires that doped by Al is lower than undoped ZnO nanowires.

5.4. Growth of ZnO/ZnInO heterostructure nanowires

In this section, the sintering method is applied to prepare a ZnO/In₂O₃ compound that became our source material. Using this material, the ZnO/ZnInO heterostructure nanowires are grown on Si(111) substrates in a conventional tube furnace. During this process, any metal catalyst is not used, instead, a carrier gas consisting of a mixture of argon and oxygen is employed. The self-catalytic role of indium in the growth process of ZnO/ZnInO heterostructure nanowires on Si(111) is investigated. A comparative study of the morphological and optical properties of ZnO/ZnInO heterostructure versus undoped ZnO nanowires is also performed using field emission scanning electron microscopy and photoluminescence spectroscopy.

5.4.1. Experimental details

ZnO/ZnInO nanowires were fabricated in a conventional horizontal furnace without using of a metal catalyst. First, Si(111) substrates were cleaned like previous process. Zinc oxide (99.99%) and indium powders (99.99%) were mixed in a molar ratio of 10:2, and then pressed into a small pill under a pressure of 15 MPa. The pill was calcined in a box furnace at 500 °C for 5 h and sintered at 900 °C for 12 h in air, transforming it into a ZnO-In₂O₃ compound. After the heat treatment, the pill was ground into powder again and mixed with commercial graphite powder in a 1:1 weight ratio. This powder was used as source material for the ZnO/ZnInO nanowires.

The source material was heated up to 950 °C and the temperature of the substrate was maintained at 600 °C during the growth process. High purity Ar and O₂ gases were fed at about 100:10 sccm into the furnace tube at one end, while the other end was connected to a rotary pump. In this manner, two set of wires were made, one using ZnO-In₂O₃ and the other using pure ZnO material. For the ZnO/ZnInO nanowires,

three growth times of 30, 50 and 90 min were tested. The other conditions are similar to previous conditions.

5.4.2. Results and discussion

Figures 5.22 (a₁-a₂) show low- (top view) and high- (side view) magnification FESEM images of the ZnO/ZnInO heterostructure nanowires respectively, grown for 90 min. In addition, Fig. 5.22 (a₁) shows a typical EDX spectrum of the nanowires. The EDX spectrum clearly reveals the presence of zinc, oxygen, and indium.

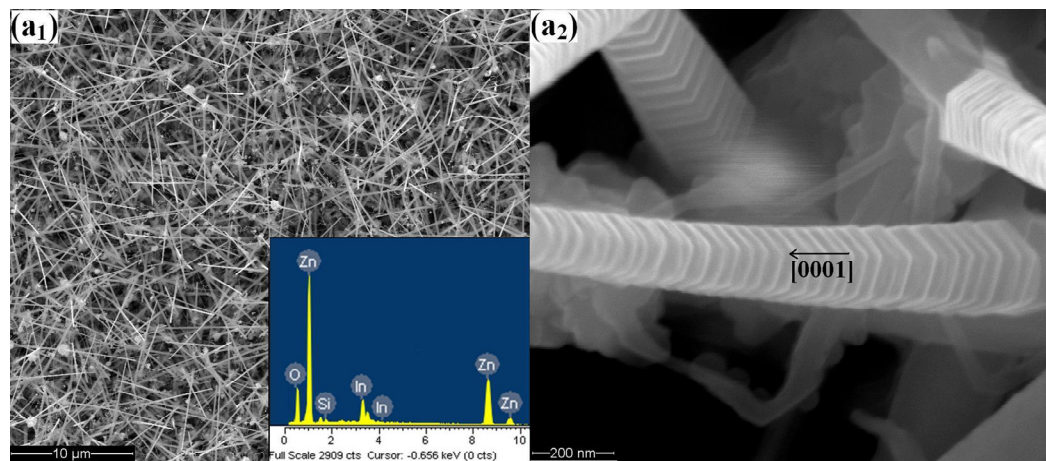


Figure 5.22. (a₁) Low-magnification FESEM image and EDX spectrum for ZnO/ZnInO heterostructure nanowires grown for 90 min. (a₂) High-magnification of a single ZnO/ZnInO heterostructure nanowire grown for 90 min. The black arrow shows that the growth direction of the nanowire is [0001].

Under high-magnification, as shown in Fig. 5.22 (a₂), these nanowires appear to have a perfect hexagonal geometry and a clearly layered structure. It appears as though the nanowire is formed by the piling of several layers of hexagonal nanocrystals that are roughly 20 to 30 nm in thickness, where each layer has a smaller area than the previous layer. Therefore, the orientation of nanowire growth is preferentially along the direction of the c-axis ([0001]) and is characterized by layered hexagonal edges.

EDX measurements are used to investigate the longitudinal indium distribution in a single nanowire. Figure 5.23 shows an FESEM image of a single nanowire with the

EDX spectra from different regions along this nanowire as follows: (A) of the tip, (B) of the upper half, (C) of the middle, and (D) of the bottom half of the ZnO/ZnInO nanowire. As is observed in the FESEM image, the nanowire is completely straight, but is tapered with a tip diameter of 90 ± 5 nm and a base diameter of 230 ± 5 nm. The indium peaks in the EDX spectra for this nanowire are not observed for the bottom half of the nanowire (D part). The length of the D part of the nanowire is about 1/3 of the nanowire length. These spectra show an increase in the percent composition of indium when moving towards to the tip of the nanowire. Several nanowires, which were randomly selected from different places on the sample, all show approximately the same shape and distribution of elements as the nanowire for which the aforementioned data was obtained.

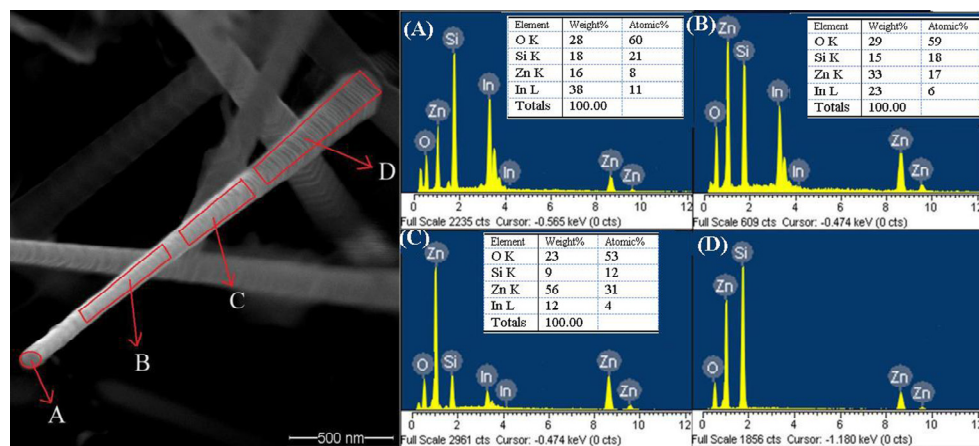


Figure 5.23. A single ZnO/ZnInO heterostructure nanowire grown for 90 min with four spectra taken of four distinct regions along this nanowire: (A) of the tip, (B) of the upper half, (C) of the middle, and (D) of the bottom half regions of the nanowire.

To understand the growth process of the nanowires in more detail, nanowires at an earlier stage of growth (50 min rather than 90 min) are examined under the same conditions described above. Figure 5.24 shows an FESEM image and an EDX spectrum of the top view of the nanowires grown for 50 min. Compared with wires grown for 90 min; these nanowires are shorter in length. Furthermore, the EDX spectrum from the top view reveals a higher concentration of indium than observed previously.

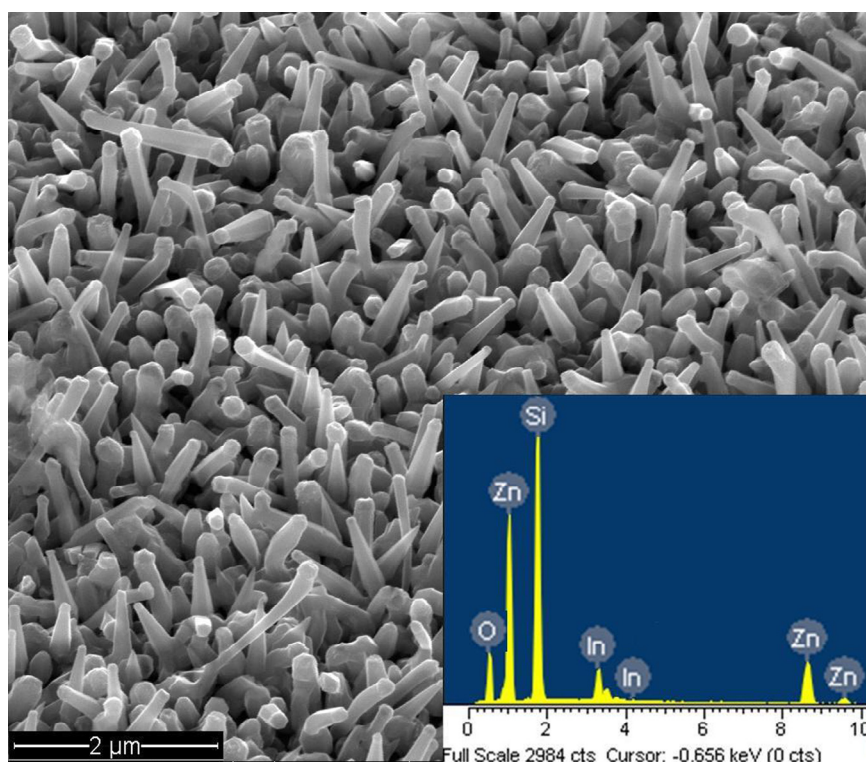


Figure 5.24. Low magnification FESEM image and EDX spectrum of the ZnO/ZnInO heterostructure nanowires grown for 50 min.

A high-magnification FESEM image of a single nanowire from this step shows that the growth direction of these nanowires is also along the c-axis, because the cross section of this nanowire is also hexagonal (Fig. 5.25). Therefore, the process of the growth at this step is evidently similar to that at later times. Moreover, the diameters of these nanowires in the base resemble the diameters of the longer nanowires. Similar to the previous analysis, a single nanowire grown for 50 min was characterized using EDX. Figure 5.25 shows the EDX spectra taken: (A) of the tip, (B) of the middle, and (C) of the bottom half regions of the nanowire. The EDX spectra of this nanowire contain indium peaks only in the middle region and at the tip of the nanowire. The percentage composition of indium increases going from the middle of the nanowire to the tip, in a manner similar to that observed in the longer nanowire.

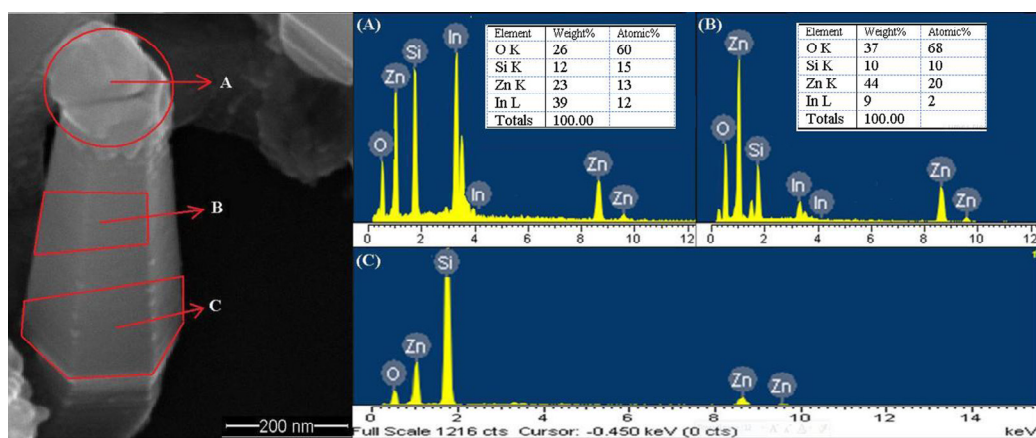


Figure 5.25. A high-magnification FESEM image of a single ZnO/ZnInO heterostructure nanowire grown for 50 min, with three spectra taken of three regions along the nanowire: (A) of the tip, (B) of the middle, and (C) of the bottom half regions of the nanowire. These spectra indicate that indium is not detected in the bottom half region of the nanowire.

Figures 5.26 (a-c) show high resolution N (E) Auger electron spectroscopy of indium, oxygen, and zinc respectively, for a single ZnO/ZnInO heterostructure nanowire. The same method that was used to classify the EDX results by location along the wire was also used for the AES results. As illustrated in Fig. 5.26 (a), an indium peak at 395 eV is only evident for the upper half part of the single ZnO/ZnInO nanowire. This corresponds to the MNN Auger electron emission from indium. By contrast, no peaks associated with indium are observed in the bottom half part of the single nanowire. These results are in agreement with the EDX results. AES spectra of the oxygen (Fig. 5.26 (b)) indicate clear peaks at 485 and 506 eV for the upper half part of the nanowire, while these peaks lie at 480 and 503 eV for the bottom half part of the nanowire. These correspond to the KLL Auger electron emission from oxygen. Finally, AES spectra for zinc, as shown in Fig. 5.26 (c), have peaks at 900, 985, and 1005 eV for the upper half part of the single nanowire and 891, 982, and 1004 eV for the bottom half part of the nanowire. These correspond to the LMM Auger electron emission of zinc.

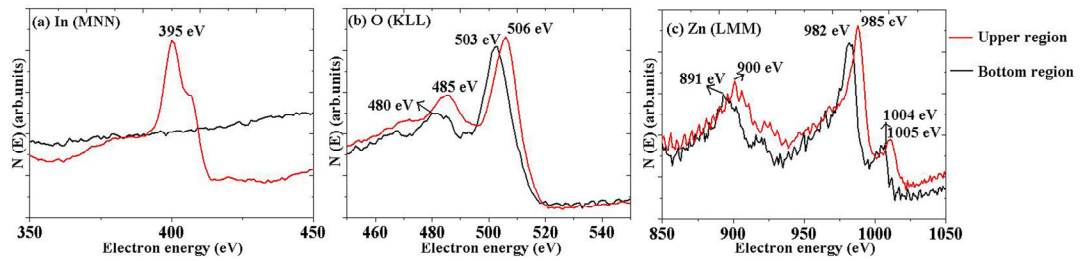


Figure 5.26. High resolution $N(E)$ Auger electron emission spectroscopy of ZnO/ZnInO heterostructure nanowires grown for 90 min, obtained from two different regions (upper and bottom half) of a single nanowire. (a) Indium spectra corresponding to the MNN Auger electron emission from indium. These spectra show that the indium element is only detectable in the upper half part of the nanowire. (b) Oxygen spectra corresponding to the KLL Auger electron emission from oxygen. (c) Zinc spectra corresponding to the LMM Auger electron emission from zinc.

$$\text{O(KLL)} \left\{ \begin{array}{l} 480 \text{ eV} \rightarrow 485 \text{ eV} \\ 503 \text{ eV} \rightarrow 506 \text{ eV} \end{array} \right. \quad \text{Zn(LMM)} \left\{ \begin{array}{l} 891 \text{ eV} \rightarrow 900 \text{ eV} \\ 982 \text{ eV} \rightarrow 985 \text{ eV} \\ 1004 \text{ eV} \rightarrow 1005 \text{ eV} \end{array} \right. \quad (5-3)$$

In the previous section, aluminum doped ZnO nanowires. We proposed that, as a good conductor, Al could increase the conductivity of the ZnO nanowires, and consequently change the Auger electrons energies of ZnO nanowires doped with Al. However, larger shifts in the peaks of zinc and oxygen were observed in the AES spectra when the nanowires were doped with Al, compared with the indium doping investigated here. It is likely that this difference between Al-doping and In-doping can be explained by the difference in electrical conductivity between Al ($\sigma = 0.377 \times 10^6$ 1/cm. Ω) and In ($\sigma = 0.116 \times 10^6$ 1/cm. Ω). All of these results indicate that ZnO/ZnInO nanowires grow with a heterostructure that involves formation of undoped ZnO as a first step and ZnInO as a second step.

To compare with the heterostructure nanowires, undoped ZnO nanowires synthesized (Fig. 5.27) under the same conditions. Unlike the heterostructure nanowires, the sides of undoped ZnO nanowires are smooth. The wires are not tapered, and they have a uniform diameter of about 80 nm on average (as shown in the inset of Fig. 5.27). Their typical length is several micrometers. Since no catalyst is used in the

growth of the ZnO nanowires in this study, the VLS mechanism is not responsible for their growth. The absence of detectable catalyst particles at the ZnO nanowire tips supports this (the inset of Fig. 5.27 shows clear tips of ZnO nanowires). It appears that the growth of the straight ZnO nanowires reported here occurs via a VS mechanism.

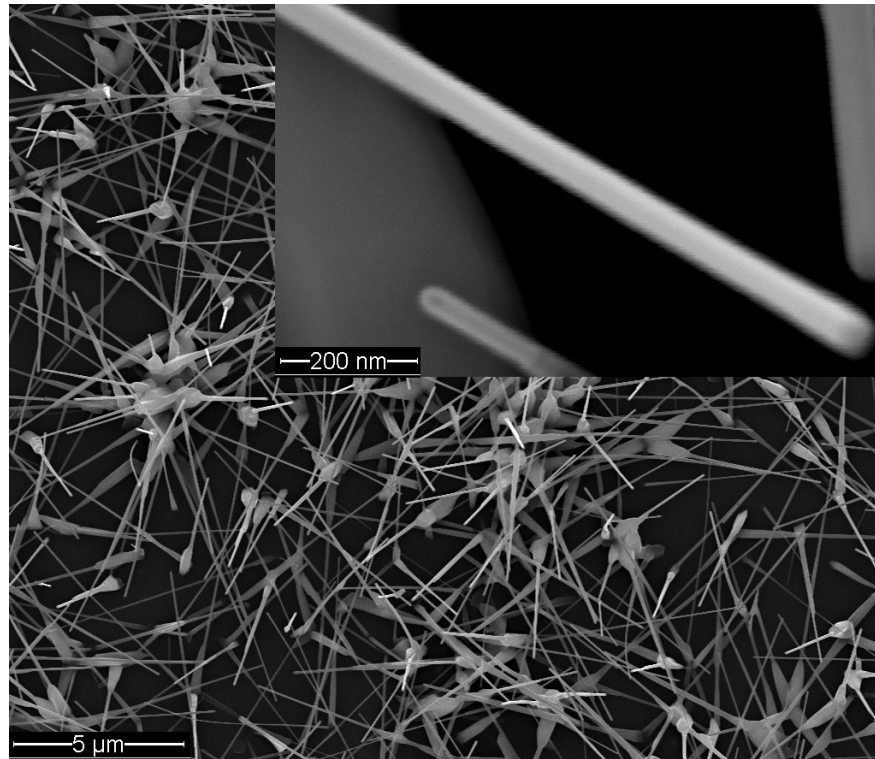


Figure 5.27. FESEM image of undoped ZnO nanowires grown under the same conditions as the ZnO/ZnInO heterostructure nanowires. The inset shows a single nanowire with smooth surface and without any metal at the nanowire tip.

To better understand the details of the growth process of the heterostructure nanowires, the source material is characterized prior to evaporation using XRD, and the materials remaining in the boat is characterized by the EDX after deposition times of 30, 50, and 90 min. Figure 5.28 shows the XRD pattern of the initial pill (ZnO-In). The pattern exhibits two phases of material, belonging to ZnO with hexagonal phase, and the other belonging to In_2O_3 with cubic phase. This implies that the sintering method is able to create a uniform composite of ZnO and In_2O_3 . Additionally, indium that mixed with

the ZnO powder reacts with atmospheric oxygen during the sintering process to form In_2O_3 .

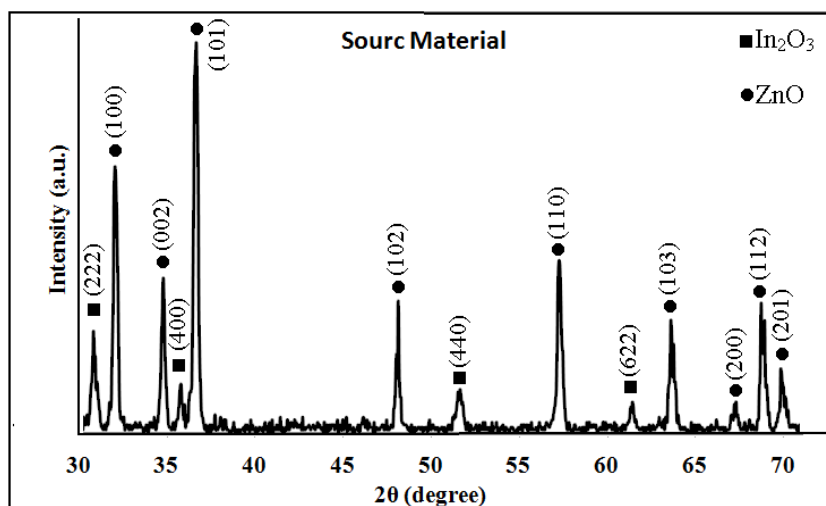


Figure 5.28. XRD pattern of the source material before evaporation.

Figure 5.29 shows the results of EDX analysis of materials remaining in the boat after evaporation. After the initial 30 minutes, much of the carbon content in the original source material remained, as did most of the zinc and oxygen. At an applied temperature of 950 °C, the ZnO powder does not evaporate although the carbon remains. In contrast, In_2O_3 can evaporate due to its lower melting point. For this reason, we observe a few deposition of ZnO nanostructures on the substrate after 30 minutes of growth. Rather, only scattered particles of indium oxide containing a small amount of zinc are deposited on the substrate (Fig. 5.30). However, after 50 minutes of growth, the carbon content in the boat is dramatically decreased. This indicates that the carbon has evaporated, and in this time frame, deposition of ZnO nanostructures on the substrate is first observed (Fig. 5.24). Indium content in the source changes more between 50 and 90 minutes because more of the zinc and oxygen content has evaporated.

Based on these results, the growth mechanism of heterostructure nanowires can be tentatively proposed. No metal as catalyst has used on the substrate, and therefore growth must be with nucleation sites. These sites are most likely established by

$\text{In}_{2x}\text{O}_{3y}$ particles ('x' and 'y' are smaller than one) because the melting temperature of $\text{In}_{2x}\text{O}_{3y}$ is smaller than that of In_2O_3 (1910 °C) or ZnO (1975 °C).

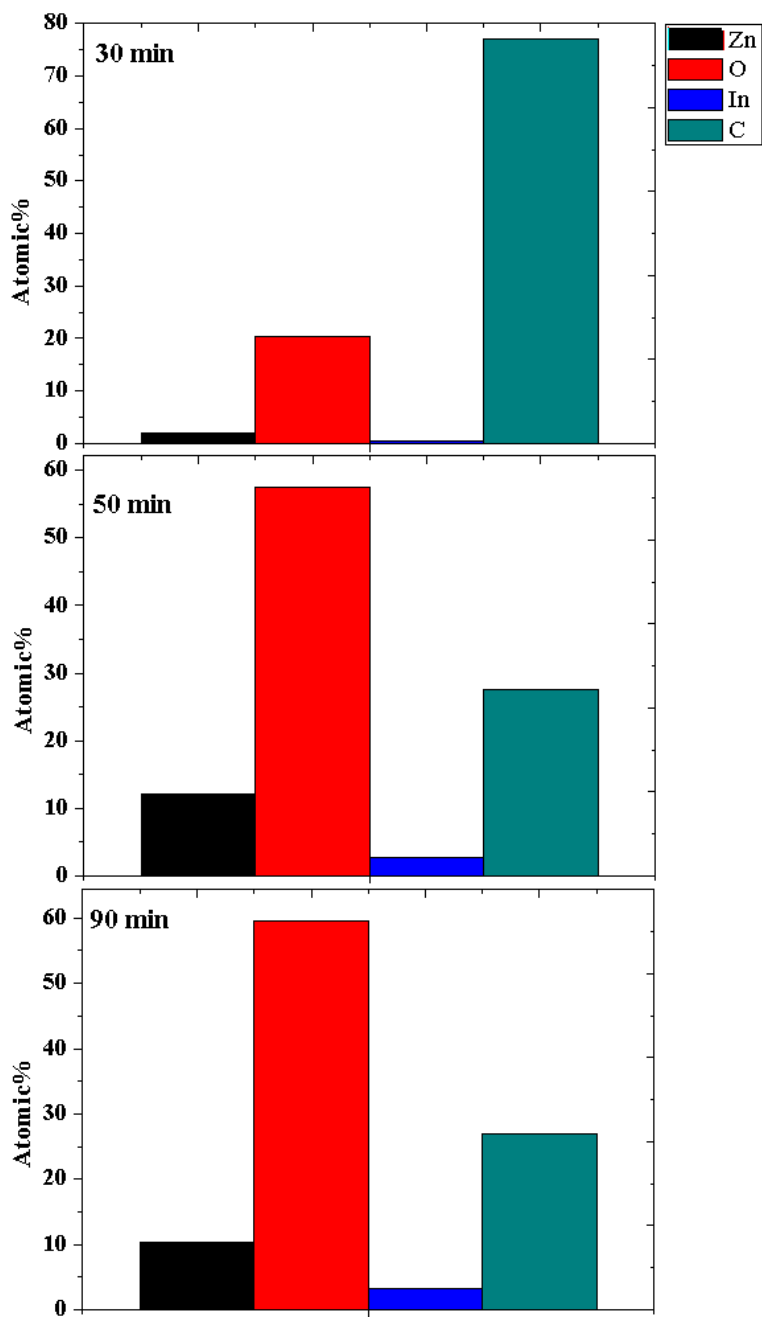


Figure 5.29. EDX results of materials remaining in the boat after 30, 50, and 90 min of evaporation. This pattern shows that the content of carbon has decreased after 30 min dramatically. Also, it shows carbon act in evaporation of ZnO .

Because the Si wafer is etched using HF acid, it has high surface roughness. Therefore, droplets of liquid $\text{In}_{2x}\text{O}_{3y}$ located on the surface clusters and serve as ideal nucleation sites. Figure 5.30 shows $\text{In}_{2x}\text{O}_{3y}$ droplets that contain a few Zn elements.

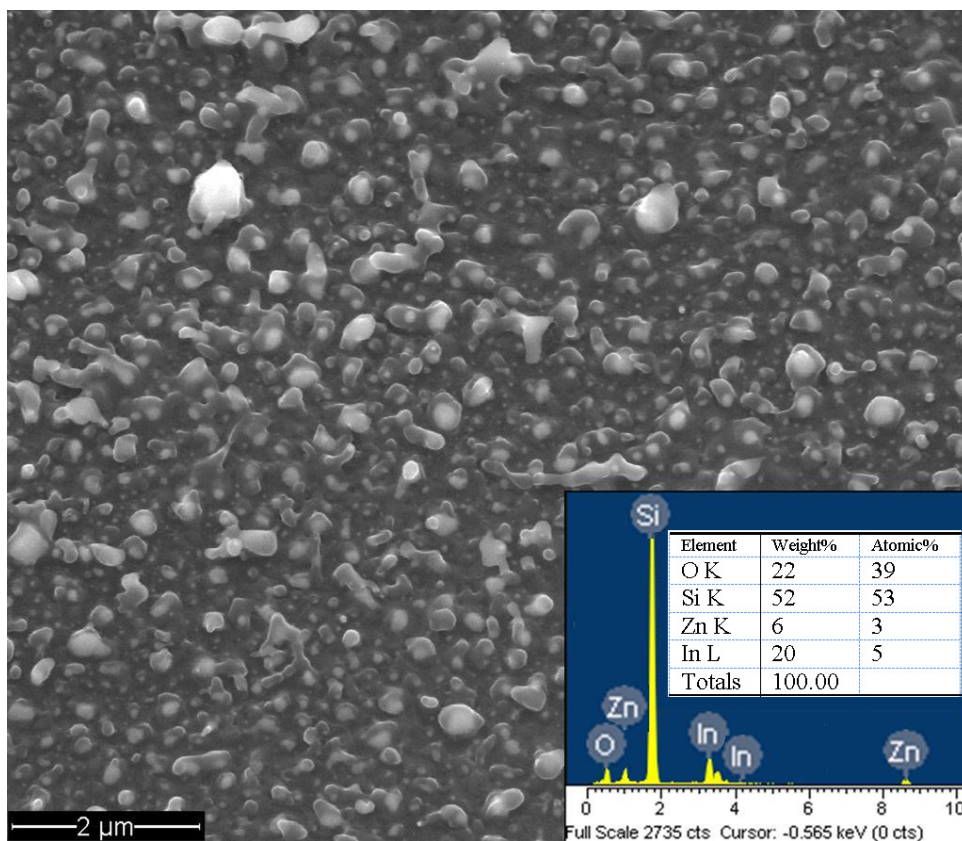


Figure 5.30. An FESEM image and EDX spectrum of the first deposition observed at 30 min.

$\text{In}_{2x}\text{O}_{3y}$ may in fact play as a self-catalytic role in the growth of the heterostructure nanowires. The FESEM results obtained from a single nanowire in Fig. 5.23 and Fig. 5.25 show the self-catalyst particles at the tips of the ZnO/ZnInO nanowires. In contrast with undoped ZnO nanowires, the growth process of the ZnO/ZnInO nanowires cannot be based on the VS mechanism. Therefore, we conclude that the unique morphology of the heterostructure nanowires may be attributed to the self-catalytic role of the indium. This supports the premise that the growth of heterostructure nanowires governed by the VLS mechanism. According to this

mechanism, the vapors of ZnO_x are absorbed by the self catalyst, reach supersaturation, and then finally solidify.

According to this explanation, the tapering of the nanowires reflects changing nanowire diameter during growth, and this is due to changes in the droplet size of the self-catalyst. During the growth process, the $\text{In}_{2x}\text{O}_{3y}$ catalyst diffuses into the nanowires. This premise is supported by the decrease in indium content from Fig 5.23 (A) to Fig 5.25 (A). Due to this diffusion, the droplet size decreases. The droplet size is the unique factor which controls the nanowires diameter, so as the growth time increases, the growing nanowires becomes thinner. This process is observed during both stages of the growth. Lin *et al.* (2007) also observed the effect of indium on the morphology of the ZnO nanowires. They observed that these nanowires have screw shape. The growth mechanism of the heterostructure nanowires, and the formation of the self-catalyst on the Si substrate, is schematically shown in Fig. 5.31.

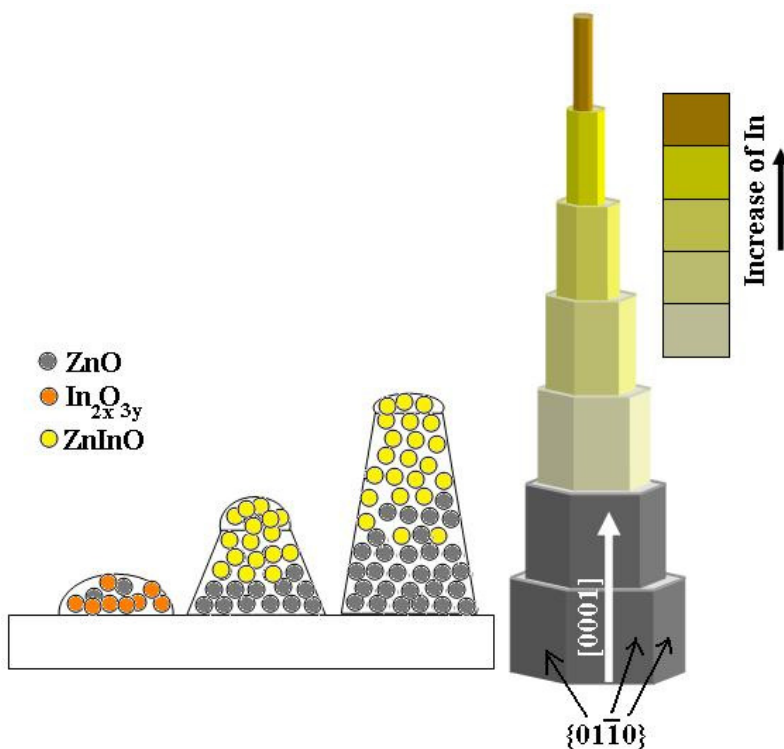


Figure 5.31. Schematic illustrating the formation of ZnO/ZnInO heterostructure nanowires and the diffusion of self-catalyst of $\text{In}_{2x}\text{O}_{3y}$ during the growth process.

Diffusion of the indium catalyst into the nanowires is also shown schematically in this figure using the colored legend.

Figure 5.32 shows XRD patterns for heterostructure nanowires and undoped ZnO nanowires grown for 90 min. The XRD patterns in Fig. 5.32 indicate the presence of a hexagonal structure and are in agreement with the results from the bulk ZnO. No peaks from Zn, In or other impurities are visible. The FWHM of the all peaks in the ZnO/ZnInO pattern are bigger than those of the undoped ZnO nanowires. This may be due to different in nanowire diameter or due to In serving as an impurity in the ZnO/ZnInO nanowires.

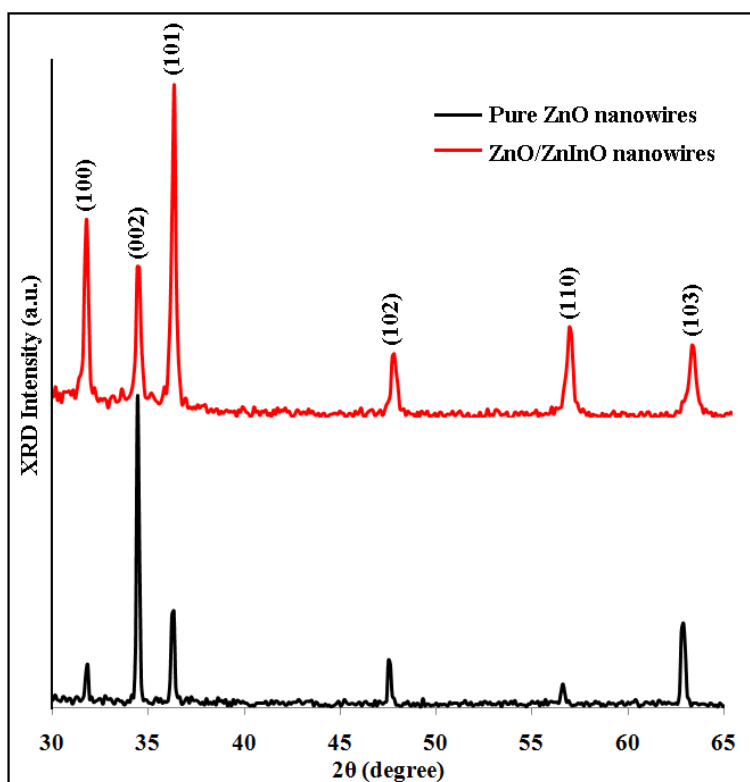


Figure 5.32. XRD patterns of ZnO/ZnInO heterostructure nanowires and undoped ZnO nanowires. Both patterns match that of bulk ZnO with hexagonal structure and no peaks from Zn, In or other impurities are detected.

PL measurements were performed to study the optical properties of the ZnO/ZnInO heterostructure nanowires and the undoped ZnO nanowires. The peaks of the UV emission for the ZnO/ZnInO heterostructure nanowires and undoped ZnO

nanowires are centered at 372 and 380 nm, respectively. Figure 5.33 shows the PL spectrum for ZnO/ZnInO heterostructure nanowires grown for 90 min, and also an analogous for undoped ZnO nanowires. As shown in Fig. 5.33, the UV peak of the ZnO/ZnInO heterostructure nanowires is blue-shifted by about 8 nm. When ZnO is doped with group-III elements such as Al, Ga, and In, the dopants are expected to act as singly charged donors by substituting for Zn. The excess carriers thus supplied to the conduction band increase the electrical conductivity of ZnO.

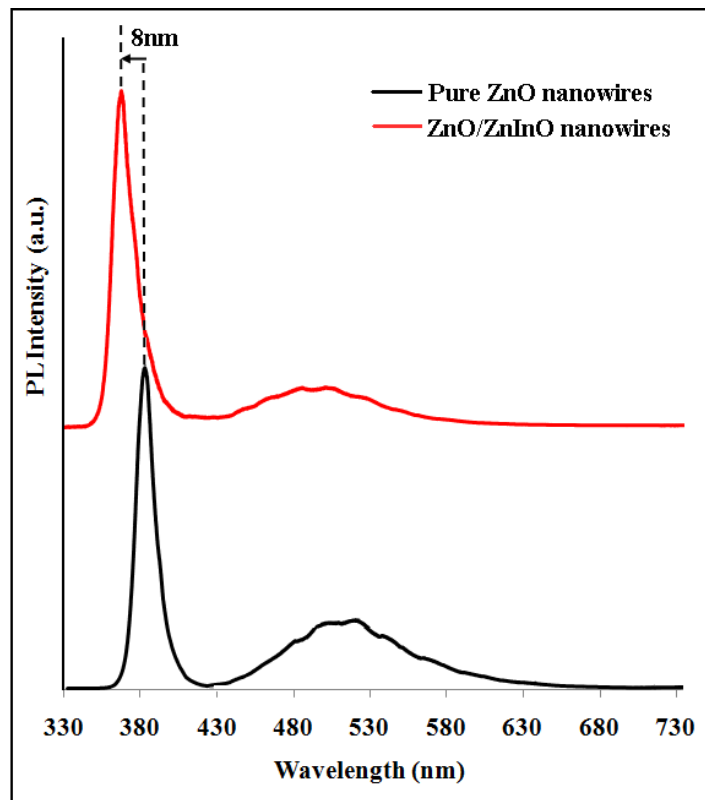


Figure 5.33. PL spectra of ZnO/ZnInO heterostructure nanowires and undoped ZnO nanowires. The spectrum of the heterostructure nanowires indicates a blue-shift in the UV peak by 8 nm for the heterostructure nanowires in comparison to undoped ZnO nanowires. This shift is attributed to the Burstein-Moss effect.

It is clearly observed Burstein-Moss effect in this sample due to In doping. The FWHM of the UV peak of the ZnO/ZnInO nanowires (37.31 nm) is bigger than that of the undoped ZnO nanowires (20.39 nm). This indicates better relative crystalline quality of the undoped ZnO nanowire. The larger FWHM of the UV peak of the ZnO/ZnInO

nanowires can be explained by the formation of band tiling in the band gap, which is often induced by the introduction of impurities into semiconductors. The UV/DLE ratios for the ZnO/ZnInO and the undoped ZnO nanowires are about 3.09 and 4.12, respectively. The smaller UV/DLE ratio for the ZnO/ZnInO nanowires is probably due to distribution of the indium along the ZnO/ZnInO nanowires. This distribution lowers crystallinity of the nanowires, and thus decreases the optical quality of the ZnO/ZnInO nanowires. Lastly, In substitution Zn atoms in the ZnO lattice can induce which can affect the PL results. In particular, the ZnO nanowires with In, exhibit a higher concentration of defects such as stacking faults, due to the different ionic radii of In^{3+} (0.08 nm) and Zn^{2+} (0.074nm). Chen *et al.*, (2005) suggested that a decrease in the UV/DLE ratio after indium doping is due to the weak exciton Coulomb interaction effect. They explained that indium atoms act as scattering centers, generating a screened Coulomb potential field, which ionizes excitons due to the loss of the Coulomb interaction effect.